

Assessing Quantitative Results in Accretion Simulations: From Local to Global

John F. Hawley, Xiaoyue Guan

*Department of Astronomy
University of Virginia
P.O. Box 400325
Charlottesville, VA 22904-4325*

`jh8h@virginia.edu; xg3z@virginia.edu`

and

Julian H. Krolik

*Department of Physics and Astronomy
Johns Hopkins University
Baltimore, MD 21218*

`jhk@pha.jhu.edu`

ABSTRACT

Discretized numerical simulations are a powerful tool for investigation of nonlinear MHD turbulence in accretion disks. However, confidence in their *quantitative* predictions requires a demonstration that further refinement of the spatial gridscale would not result in any significant change. This has yet to be accomplished, particularly for global disk simulations. In this paper, we combine data from previously published stratified shearing box simulations and new global disk simulations to calibrate several quantitative diagnostics by which one can estimate progress toward numerical convergence. Using these diagnostics, we find that the established criterion for an adequate numerical description of linear growth of the magneto-rotational instability (the number of cells across a wavelength of the fastest-growing vertical wavenumber mode) can be extended to a criterion for adequate description of nonlinear MHD disk turbulence, but the standard required is more stringent. We also find that azimuthal resolution, which has not often been extensively examined in previous studies, can significantly affect the evolution of the poloidal magnetic field. We further analyze the comparative resolution requirements of a small sample of initial magnetic

field geometries; not surprisingly, more complicated initial field geometries require higher spatial resolution. Otherwise, they tend to evolve to qualitatively similar states if evolved for sufficient time. Applying our quantitative resolution criteria to a sample of previously published global simulations, we find that, with perhaps a single exception, they are significantly under-resolved, and therefore underestimate the magnetic turbulence and resulting stress levels throughout the accretion flow.

Subject headings: Black holes - magnetohydrodynamics (MHD) - stars:accretion
- methods: numerical

1. Introduction

Numerical simulation is an important tool for understanding the dynamics and evolution of accretion disks. In the last decade, the increase in computational power has made it possible to carry out global disk simulations of increasing complexity, as the state-of-the-art has risen from pseudo-Newtonian dynamics (Hawley & Krolik 2001; Machida & Matsumoto 2003) to full three-dimensional general relativistic physics (De Villiers & Hawley 2003; Gammie et al. 2003; Aninos et al. 2005), most recently including toy-model thermodynamics (Noble et al. 2009; Shafee et al. 2008). These simulations already have several achievements to their credit. They have shown that the magneto-rotational instability (MRI; Balbus & Hawley 1991, 1998) can be effective in providing the required internal stress. They have shown that disks rapidly evolve to a near-Keplerian distribution of angular momentum regardless of the initial angular momentum distribution. They have demonstrated two mechanisms by which a large-scale field magnetic field can be attached to a black hole, either inward transport of truly large-scale field (Beckwith et al. 2009) or spontaneous, if temporary, inflation of field loops within the accretion flow (McKinney & Gammie 2004; De Villiers et al. 2003, 2005). If the black hole rotates, these large-scale fields can support Poynting flux-dominated jets.

Nonetheless, a number of questions remain open regarding the *quantitative* quality of the predictions these simulations can make for real black holes in Nature. Some of these questions have to do with the adequacy of the physical approximations made, most notably the still rather crude account of thermodynamics in even the best of them. Radiation forces, although likely very important in numerous black hole accretion contexts, likewise remain largely omitted in global simulations. Others have to do with physical choices that must be made in order to calculate anything, but about which we have no real knowledge, particularly the initial strength and structure of the magnetic field. Confidence in the saturation strength of the field is greatest when it is statistically time-steady, yet very different from

its initial state. It is therefore desirable to begin with a weak magnetic field and let the natural dynamics of the situation strengthen it. Although there have been discussions in the literature that a certain initial field geometries are “most natural” (e.g., multiple loops Shafee et al. 2008), all such arguments appear to be based on little more than subjective aesthetic judgments. We might hope that these choices have little effect on the outcome, but that must be demonstrated; in the case of jet-launching, we already know that magnetic field geometry plays a major role (Beckwith et al. 2008a).

Other questions have to do with the specifics of the numerical techniques employed. Every algorithm has certain strengths and weaknesses, and their impact depends on the nature of the problem being simulated. Geometric symmetry conditions may be imposed (e.g., imposing azimuthal boundary conditions periodic across a wedge rather than around a full circle in order to economize on computer time) whose consequences cannot easily be determined *a priori*. Transients due to arbitrary initial conditions must be eliminated. And every discrete numerical scheme must be shown to have fine enough resolution, both spatially and temporally, to describe adequately the physical processes involved. This last point is a special concern for accretion simulations because MHD turbulence is essential to the story, but true microphysical dissipation operates on a scale so many orders of magnitude smaller than the disk scale that no conceivable simulation can hope to resolve it. It is these more technical questions that are the province of this paper.

In this paper, we will by no means attempt a full comparison of a broad range of codes and algorithms. We will, however, present some comparative data in the shearing-box context in order to estimate the potential level of contrast in saturated stress and other properties among codes utilizing different algorithms run at similar resolutions.

We will also pass over the second question, that of overly-restrictive symmetry conditions. We will only note that Schnittman et al. (2006) showed that in a full- 2π simulation there is substantial power in stress fluctuations on azimuthal scales as long as ~ 1 radian. Given that finding, wedges of at least a quarter-circle are certainly required.

The third question, how to eliminate transients, poses somewhat different issues, depending upon whether the context is stratified shearing-boxes or global disks. In the former case, it has long been established (Hawley et al. 1995) that the principal transients are erased in ~ 10 orbits, but the turbulence exhibits significant long-term, chaotic fluctuation power (Winters et al. 2003), even over durations as long as the very longest simulations, $\gtrsim 500$ orbits. Nonetheless, despite the long-term variability, it is possible to define time-averages reasonably well. We will discuss quantitative definition of transient removal in global disk simulations more fully in § 5. Here it suffices to say that statistical stationarity in global simulations has a dual meaning. One sense is the same as for shearing-boxes: given a surface

density and an orbital shear, the system should achieve a statistical steady-state in the amplitude of the MHD turbulence. The other sense is that the local surface density must have a well-defined mean value over some period of time. This is more difficult, and can never be achieved over the entire simulation volume.

The fourth and last question, how to determine whether a given simulation has adequate resolution to return accurate quantitative results, will occupy most of our attention. One expects convergence of the numerical solution to an exact solution as the grid size goes to zero, i.e., $\Delta x \rightarrow 0$. Since that limit is never attained, convergence generally refers to the observation that a given quantity approaches some fixed value as Δx is reduced. Different quantities, of course, have different convergence rates (in practice, the formal convergence rate, determined by the order of the scheme, need not be manifest at a given finite resolution), and individual quantities may themselves be subject to several different criteria. The issue of convergence is further complicated when evolving equations without explicit resistivity and viscosity. In that case, dissipation occurs at the grid scale, and the effective Reynolds number of the system becomes a function of resolution.

As an illustration, consider the central quantity of accretion physics, the local stress. Its saturation depends on the interplay between several different processes. First, small magnetic fluctuations are amplified by the MRI; the spatial resolution must therefore be great enough that the fastest-growing linear modes—for both poloidal and toroidal fluctuations— e -fold at the correct rate. Next, nonlinear couplings between different wave modes must also be described properly. Adequate resolution for this process depends upon the lengthscale of the shortest important modes, but it is hard to determine *a priori* what that lengthscale may be. Finally the turbulence must be dissipated at scales much less than the stirring scale. Lesur & Longaretti (2010) argue that in feasible simulations, *all* resolvable wavelengths are coupled together by non-linear processes. They also argue, however, that in real disks the range of non-local coupling in wavevector space is much smaller than the dynamic range between the stirring scale and the physical dissipation scale, permitting the creation of a genuine inertial range.

Initial conditions may also play a role in determining the necessary resolution. Because the fastest-growing MRI wavelength is proportional to the field strength parallel to the wavevector, the weaker the initial field, the finer the spatial resolution must be. In the non-linear stage when the magnetic field has a fixed large-scale element, even modest resolution suffices to describe that portion reasonably well, although a full description of the turbulence places stronger demands. On the other hand, when even the largest scales maintained by the physics are smaller, the minimum necessary resolution becomes correspondingly finer. Popular initial conditions for zero net-flux magnetic field configurations illustrate this effect.

When the initial magnetic field is a single set of nested poloidal loops, many of these field line loops become attached to the black hole horizon, forming a radially large-scale magnetic structure linking the black hole and the disk. On the other hand, when the initial field is quadrupolar, with a pair of nested poloidal loops on either side of the midplane, these loops are free to shrink in size, demanding a much finer spatial grid if excessive resistive losses are to be avoided.

For reasons of practicality, simulators tend to choose resolutions that are as fine as possible while still consistent with their computing budget. It is therefore often not feasible to test directly for convergence by performing a new simulation with more gridzones. Although some sense of the rate of convergence can be obtained by computing models at lower resolution, that procedure would not reveal the failure of the highest resolution simulation to resolve some important feature—it is entirely possible that the reason the results do not change appreciably with changing resolution is that even the best-resolved case is incapable of sustaining an important physical effect.

Our approach to these problems is to begin with shearing-box calculations, in which it is generically easier to reach high resolution than in global disk simulations. We will search for quantities related to, but different from, the stress and that scale with resolution in a way that can be calibrated. With these in hand, it becomes possible to gain some idea of how far along the path toward convergence a global simulation has reached. We will apply these measures both to a number of older simulations and to some new ones we have carried out especially for this purpose. Full general relativity is not necessary to achieve these goals because the saturation of MHD turbulence is an essentially Newtonian process. Consequently, it is sufficient to carry out simulations using the simpler and less computationally demanding *Zeus* algorithm and a pseudo-Newtonian potential.

2. Numerical Setup and Initial Conditions

In this study we explore some of the effects of resolution and initial conditions first by examining the results from local stratified shearing box simulations, and then by computing a series of global accretion simulations. The shearing box results are, in all but two cases, taken from the literature. Our sample features several resolutions, box sizes, and numerical algorithms. Some of the numerical aspects of those simulations are described in §3; for a detailed account the reader should consult the papers where these simulations were originally presented.

Here we describe the numerical setup for the global accretion simulations carried out

specifically for this paper. As we will be focusing on the body of the disk itself rather than the interactions with the black hole or any jets or winds that form, it is sufficient to use non-relativistic MHD and to work in the pseudo-Newtonian potential to approximate the gravity of a black hole. We evolve the equations of Newtonian MHD in cylindrical coordinates (R, ϕ, z) ,

$$\frac{\partial \rho}{\partial t} + \nabla \cdot (\rho \mathbf{v}) = 0 \quad (1)$$

$$\rho \frac{\partial \mathbf{v}}{\partial t} + (\rho \mathbf{v} \cdot \nabla) \mathbf{v} = -\nabla \left(P + \mathcal{Q} + \frac{B^2}{8\pi} \right) - \rho \nabla \Phi + \left(\frac{\mathbf{B}}{4\pi} \cdot \nabla \right) \mathbf{B} \quad (2)$$

$$\frac{\partial \rho \epsilon}{\partial t} + \nabla \cdot (\rho \epsilon \mathbf{v}) = -(P + \mathcal{Q}) \nabla \cdot \mathbf{v} \quad (3)$$

$$\frac{\partial \mathbf{B}}{\partial t} = \nabla \times (\mathbf{v} \times \mathbf{B}) \quad (4)$$

where ρ is the mass density, ϵ is the specific internal energy, \mathbf{v} is the fluid velocity, P is the pressure, Φ is the gravitational potential, \mathbf{B} is the magnetic field vector, and \mathcal{Q} is an explicit artificial viscosity of the form described by Stone & Norman (1992). To model a black hole gravitational field we use the pseudo-Newtonian potential of Paczyński & Wiita (1980) which is

$$\Phi = -\frac{GM}{r - r_g}, \quad (5)$$

where r is spherical radius, and $r_g \equiv 2GM/c^2$ is the “gravitational radius,” akin to the black hole horizon. For this potential, the Keplerian specific angular momentum (i.e., that corresponding to a circular orbit) is

$$l_{kep} = (GMr)^{1/2} \frac{r}{r - r_g}, \quad (6)$$

and the angular frequency $\Omega = l/R^2$. The orbital period at a radius r is $P_{orb} = 2\pi\Omega^{-1} = 2\pi r^{3/2}(r - r_g)/r$. The innermost stable circular orbit (ISCO) is located at $r_{ms} = 3r_g$. We use an adiabatic equation of state, $P = \rho\epsilon(\Gamma - 1) = K\rho^\Gamma$, where P is the pressure, ρ is the mass density, ϵ is the specific internal energy, K is a constant, and $\Gamma = 5/3$. Radiation transport and losses are omitted. Since there is no explicit resistivity or physical viscosity, the gas can heat only through adiabatic compression or by artificial viscosity which acts in shocks, including weak shocks found in the turbulence.

The code used is a time-explicit Eulerian finite-differencing *Zeus* code for MHD (Stone & Norman 1992a; Stone & Norman 1992b; Hawley & Stone 1995).¹ We set $GM = c = 1$, so

¹Here the term *Zeus* refers to the algorithm rather than a specific code implementation. There are several publicly available versions of *Zeus* as well as a large number of individually developed versions, such as was employed here.

that $r_g = 2M$. Time and distance units are given in terms of the mass M .

The initial conditions consist of an orbiting gas torus with an angular momentum distribution parameter $q = 1.65$ ($\Omega \propto R^{-q}$), and $K = 0.0034$. The pressure maximum radius is $R = 35M$ and the inner torus edge is at $20M$. The orbital period at the pressure maximum is $1227M$. Using the definition of scale height H' in terms of the density moment, $H'/R = 0.1$ at the pressure maximum. Explicitly fitting a Gaussian function $\propto \exp[-(z/H)^2]$ to the vertical pressure distribution gives a value of $H/R \approx 0.16$. Note that $H = \sqrt{2}H_G$, where H_G is more commonly regarded as the Gaussian scale height. In an isothermal thin disk, $H_G = c_s/\Omega$. In internal code units the initial mass of the torus is 6096 (assuming a full 2π azimuthal domain; the actual computational domain runs from 0 to $\pi/2$). Of this total mass, 19% lies inside of $R = 35M$.

We use two initial field configurations and two average field strengths. The first is the standard dipole loop, in which the vector potential is written in the form

$$A_\phi = C(\rho - \rho_{cut}) \quad (7)$$

so that the field lines run along contours of constant density. Here C is a constant that sets the overall field strength and is set to zero wherever $\rho < \rho_{cut}$. This configuration is referred to as “one-loop.” We initialize a “two-loop” simulation using the vector potential function of Shafee et al. (2008), namely

$$A_\phi = [(\rho - \rho_{cut})r^{0.75}]^2 \sin[\ln(r/S)/T] \quad (8)$$

where r is the spherical coordinate radius, ρ_{cut} is set at 20% of the density maximum (thus confining the initial field to well within the edge of the initial torus), $S = 1.1r_{in}$, where $r_{in} = 20M$ is the initial inner edge of the torus, and $T = 0.16$ (see Fig. 1). For either geometry, the initial field strength is normalized to a β value, either 100 or 1000, defined as the ratio of the total volume-integrated gas pressure to the volume-integrated magnetic pressure.

Boundary conditions are periodic in ϕ and outflow along the z and R boundaries. One consequence of cylindrical coordinates and our use of an inner boundary radius located at $R_{in} > r_g$, is that there is a cutout parallel to the z -axis through which matter as well as field can pass and leave the grid. Therefore, in these simulations no large-scale field can become attached to the black hole or fill the axial region as is seen in the GR simulations. Because the focus here is on the evolution of the disk away from the black hole and plunging region, we accept this limitation for the sake of concentrating computational power on the torus itself.

The grid used in this study is designed to place as many zones as possible within the main body of the accretion disk. The inner boundary of the radial grid is set at $R_{in} = 4M$. From

there it runs outward with constant ΔR to R_1 , beyond which $\Delta R/R$ is set to a constant. This definition produces a logarithmically stretched grid throughout most of the domain while avoiding overly small ΔR values near the inner boundary. The z grid concentrates half of the total number of zones symmetrically around the equator using equal Δz . This portion of the grid extends to $z = \pm z_1$ from the equator. The remaining z zones are logarithmically stretched outward to boundaries that are well-removed from the initial torus. The ϕ grid uses evenly spaced zones that span one quarter of the full 2π .

We choose a fiducial grid, Grid M (“medium resolution”) and vary the resolution relative to it. Grid M contains 256 radial zones with 48 zones inside of $R_1 = 20M$. The outer radial boundary is at $R = 253M$. The z grid uses 288 zones with 144 grid zones covering the range $|z| \leq z_1 = 5M$. Using the density moment definition of the scale height, $H' \sim 3.3M$ at the location of the pressure maximum, giving ~ 48 z zones per H' . Outside of $z = \pm 5M$ the grid is logarithmically stretched out to $z = \pm 54M$. The ϕ grid uses 64 equally-spaced zones. In the inner disk (i.e., $6M \leq R \leq 20M$ and $|z| \leq 5M$), the cell aspect ratio $\Delta R/\Delta z = 4.8$ and $\Delta R/(R\Delta\phi) = 2.3$ – 0.68 (from $R = 6M$ to $R = 20M$).

The simulations performed on Grid M will be contrasted with the results obtained using other grid resolutions. The lower resolution Grid L (“low resolution”) is half as well resolved in R and z . It consists of 128 radial zones with 24 equally spaced zones between $R = 4M$ and $20M$, with ΔR increasing $\propto R$ from that radius out to $R = 253M$. At the pressure maximum, $\Delta R = 1.07M$. The z grid has 144 zones, half of which are concentrated inside $z = \pm 5M$, where the minimum Δz is $0.139M$. The ϕ grid is the same as in Grid M. In this case, $\Delta R/\Delta z = 4.8$ as for Grid M, but $\Delta R/(R\Delta\phi) = 4.5$ – 1.4 .

Grid R (“high-R resolution”) is the same as Grid M for z and ϕ , but the number of radial zones is increased to 816. Inside $R_1 = 10M$, $\Delta R = 0.04M$; outside that radius, $\Delta R/R = 0.004$. The outer boundary of the radial grid is located at $R = 142M$. Its cell aspect ratios are $\Delta R/\Delta z = 0.58$ – 1.2 (once again, from $R = 6M$ to $R = 20M$) and $\Delta R/(R\Delta\phi) = 0.27$ – 0.16 .

Two other grids are used to study the influence of the ϕ resolution. In Grid PL, the number of ϕ zones is reduced to 32. It uses 256 R zones, but redistributes them to decrease ΔR . For this grid, $\Delta R = 0.125M$ inside of $R = 10M$, and $\Delta R/R = 0.0124M$ outside that point. Grid PH is the same as Grid M but with the number of ϕ zones increased to 128.

We employ a variety of diagnostics to analyze the simulations. Certain quantities, such as total magnetic and kinetic energies, are computed and recorded every 10 timesteps. We also save binary data files and compute integrals of quantities over cylindrical shells at regular time intervals.

3. Shearing Boxes and Resolution Diagnostics

To quantify the resolution effects in global simulations we begin with the shearing box (Hawley et al. 1995), a system where greater effective resolution can be employed and more extensive resolution studies are possible. Since shearing box models were first introduced, many studies have been carried out to measure how the stress levels depend on resolution, the initial field strength and geometry, and other thermodynamic factors (e.g., Hawley et al. 1995, 1996; Brandenburg et al. 1995; Stone et al. 1996; Fleming et al. 2000; Miller & Stone 2000; Sano & Inutsuka 2001; Sano & Stone 2002; Sano et al. 2004; Fromang & Papaloizou 2007; Simon et al. 2009) The first shearing box simulations employed comparatively few total zones (e.g., $32 \times 64 \times 32$ zones in x, y, z), but recently the number of zones used in simulations has substantially increased.

Resolution studies using stratified shearing boxes that include the vertical component of gravity are the most relevant for comparison to global simulations. We have examined data from several recent stratified shearing box resolution studies (Simon et al. 2011; Shi et al. 2010; Davis et al. 2010; Guan & Gammie 2011) to see what, if any, general properties of the MRI turbulence might prove sensitive to resolution. Although shearing box simulations have found that the magnitude of a physical resistivity and viscosity as well as their ratios can have a significant impact on the turbulence levels (e.g. Fromang et al. 2007; Lesur & Longaretti 2007), at least for smaller magnetic Reynolds numbers (Oishi & MacLow 2011), nearly all global simulations done to date have used only grid-scale dissipation. Therefore, we consider here only those shearing box simulations without explicit (physical) small-scale dissipation. The resolutions in these simulations range from 16 to 128 zones per scale height H . The Simon et al. and Davis et al. models have an isothermal equation of state and make use of the *Athena* code with the HLLD-flux solver (Stone et al. 2008; Stone & Gardiner 2010), but differ in regard to the initial magnetic field and box size. The Davis models use a zero-net vertical field initial condition and a box that is $H : 4H : 4H$ ($x : y : z$), while the Simon models have a net toroidal field overlaid with a poloidal field loop and a box that is $2H : 4H : 8H$ ($x : y : z$); in both cases, $H \equiv \sqrt{2}c_s/\Omega$. The Shi et al. models have the same initial field configuration as Simon, but use a *Zeus* code and include heating and radiative transport. Their box had side lengths $2H' : 8H' : 16H'$ ($x:y:z$). The Guan & Gammie (2011) models use a *Zeus* code, an isothermal equation of state, and focus on larger stratified boxes; their fiducial simulation has a domain of $16H : 20H : 10H$. Table 1 presents some time-averaged data collected from Simon et al. (2011), Shi et al. (2010), Davis et al. (2010), and Guan & Gammie (2011) along with two unpublished 8 and 16 zones/ H simulations (Simon, private communication). Note that the Shi et al. data use a time-averaged scale height because the temperature in their simulations varies as determined by thermal balance between dissipation of the turbulence and radiative cooling.

It is immediately clear that resolution can strongly affect the quantity most important to disk evolution, the magnetic stress. Results from four stratified shearing box simulations that use 64, 32, 16 and 8 zones per H for the first 150 orbits are shown in Figure 2. The plotted quantity is the volume-averaged stress parameter α , defined

$$\alpha = \frac{\langle(\rho v_x \delta v_y - B_x B_y / 4\pi)\rangle}{\langle\rho\rangle c_s^2} \quad (9)$$

The 64 and 32 zone simulations are the 64Num and 32Num models of Simon et al. (2011); the 16 and 8 zone simulations are lower resolution versions of those simulations (Simon, private communication). All four simulations show initial growth to a peak that occurs at around 10 orbits in time. After this point, the 8 zone simulation (the lowest curve) clearly dies out. Large temporal variations characterize the other simulations. The stress in the 16 zone run, for example, declines slowly for the first 50 orbits, but then rises by a factor of 3 by orbit 60. The 32 and 64 zone runs maintain a time-averaged α that is consistent with the initial peak value. The 16 zone run also varies strongly with time, but with a mean *alpha* that is less than in the 32 zone run. Simon et al. (2011) note that in unstratified simulations the time-averaged α changes by a larger amount in going from 16 to 32 zone resolution than in going from 32 to 64 zones per H (their Figure 1). In both the Davis et al. and Shi et al. resolution studies, the smallest number of cells per scale height was $\simeq 20$ –30, and there is little change in α when finer resolutions are employed, including the best-resolved Davis et al. simulation, in which there are 128 cells per scale height. In Guan & Gammie (2011) the value of α went from 0.013 to 0.023 when the resolution of their fiducial model was doubled, a change from 13 to 26 zones per H in the vertical direction.

The converged value of α in these particular stratified isothermal shearing boxes is of order $\simeq 0.02$. There are, of course, additional effects beyond resolution that determine α . As discussed above, resistivity and viscosity can have a significant impact. At the same resolution, Simon et al. find consistently larger values of the stress compared to Davis et al., sometimes by close to a factor of two. The Simon et al. box is a factor of two larger in both the x and z dimensions. The Guan & Gammie (2011) simulations also provide some evidence that α can be larger when larger domains are used. There is evidence from unstratified shearing boxes that taller boxes also promote stronger magnetic field (Stone, private communication). The Shi et al. simulations, in which the equation of state directly balances heating and radiative cooling, suggest that α may be somewhat larger when more realistic thermodynamics are employed.

Even using the local shearing box, few simulations are carried out with resolutions as fine as 128 cells per scale height, so in practice one often asks the question, “In this particular simulation with only modest resolution, how close is the measured value of stress to the

numerically converged value?” Because high-resolution simulations can be very expensive in computer time, it is useful to define metrics of simulation quality that can be calibrated to a set of standard simulations and then applied to the data of a new simulation. In this way, how close that simulation comes to convergence may be estimated without the expense of additional, higher resolution simulations. In the remainder of this section, we discuss several such quantities.

3.1. Convergence metric #1: Q_z

The first such metric comes from the linear theory of the MRI. Noble et al. (2010) used the vertical field characteristic MRI wavelength to compute a quality parameter Q_z defined by

$$Q_z = \lambda_{MRI}/\Delta z = \frac{2\pi|v_{az}|}{\Omega\Delta z}, \quad (10)$$

where v_{az} is the z component of the Alfvén speed. The characteristic wavelength λ_{MRI} is close to, but not precisely equal to, the fastest growing MRI wavelength. Wavelengths $\lambda < \lambda_{MRI}/\sqrt{3}$ are stable, while all wavelengths $\lambda > \lambda_{MRI}$ are unstable, albeit with reduced growth rates $\propto (\mathbf{k} \cdot \mathbf{v}_{az})$. On the basis of unstratified shearing box simulations, Sano et al. (2004) suggested that a Q_z value greater than 6 was required in order to achieve a linear growth rate close to the analytic prediction. Considering an isothermal thin disk with only vertical field in the initial condition, λ_{MRI} can be rewritten in terms of the plasma β by noting that $\beta = 2\rho H^2 \Omega^2 / B^2$, and hence $\lambda_{MRI} = 2\pi H \beta^{-1/2}$. Thus, a value of Q_z of ~ 10 requires $1.6\beta^{1/2}$ zones per H when the field is purely vertical; when the field has any other sort of geometry, β in this expression should be scaled by the fraction of the field energy in the vertical component, giving a zone total of

$$N_z \simeq 16 (\beta/100)^{1/2} (\langle v_A^2 \rangle / \langle v_{Az}^2 \rangle)^{1/2} (Q_z/10) \quad (11)$$

per scale height H . Because the fraction of the magnetic energy in vertical field is often only ~ 0.01 – 0.1 , the number of zones required for a given β increases by ~ 3 – 10 .

The second column of Table 1 shows the values of Q_z , averaged over the midplane region ($|z| \leq 0.5H$) for our stratified shearing box simulation sample. It is necessary to pick out the midplane region because $|v_{Az}|$ generically increases sharply away from the midplane. Consequently, in these simulations in which the vertical resolution is uniform (unlike typical global simulations), Q_z generally increases by 1–2 orders of magnitude from $z = 0$ to $z \simeq 3H$. These regions with better effective resolution can be important in maintaining the turbulence. By $|z| = 2$ – $3H$, $\beta \leq 1$, and the MRI is largely suppressed and the large values of Q_z are less relevant. Comparing the Davis et al. series with the Simon series, we see that even

with 32 cells per scale height, the Sano et al. criterion is met only marginally. Although α increases dramatically when Q_z rises past a few, its dependence on resolution (in relative terms) appears to level out in the range $10 \lesssim Q_z \lesssim 20$.

3.2. Convergence metric #2: Q_y

Maintenance of poloidal field and turbulence requires non-axisymmetric motion. To estimate how well non-axisymmetric stirring is described by the simulation, we can define a merit parameter Q_y based on the toroidal field and the y grid zone size (Q_ϕ and $R\Delta\phi$ for global simulations). The toroidal field MRI is nonaxisymmetric, and the linear properties of those nonaxisymmetric modes are somewhat different from those of the vertical field MRI. Although the nonaxisymmetric MRI modes depend on toroidal field, the presence of weak poloidal components can greatly increase the total amplification of nonaxisymmetric modes beyond what is predicted for a purely toroidal field (Balbus & Hawley 1992). Like the case of vertical wavevectors, the maximum linear growth rate occurs for wavelengths comparable to the distance an Alfvén wave travels in one orbit, but mode growth also depends on the radial wavelength, which evolves due to shear. Further, maximum growth also demands vertical wavenumbers k_z much greater than H^{-1} (Balbus & Hawley 1992). For shearing box simulations, the number of y zones required to achieve $Q_y \sim 10$ is

$$N_y \sim 64 (H/4) (\beta/100)^{1/2} (Q_y/10) \quad (12)$$

for a y direction spanning $4H$. For toroidal modes in global simulations, $Q_\phi = 2\pi H/(\beta^{1/2}R\Delta\phi)$, where β includes only the toroidal field component. To resolve linear growth of the toroidal MRI in a full 2π simulation requires

$$N_\phi \simeq 1000 (0.1 R/H) (\beta/100)^{1/2} (Q_\phi/10) \quad (13)$$

azimuthal cells.

The simulations described in Table 1 are nearly all well-resolved by the Q_y criterion; this is one of the advantages of shearing boxes. Only in one case (the Simon 8 cells per H run) is $Q_y < 10$. In both the Davis et al. and Simon et al. simulations, the cells are cubical. Because shear ensures that the azimuthal component of the magnetic field is much stronger than the vertical component, cell sizes that are too coarse to yield good vertical resolution can nonetheless be quite adequate to describe azimuthal behavior. However, in simulations whose grids are elongated in the azimuthal direction, Q_y values will be smaller. In the better-resolved Davis and Simon simulations for example, $Q_y/Q_z \sim 4$ and one might expect that if $\Delta y/\Delta z \sim 4$, Q_y would be only comparable to Q_z .

3.3. Convergence metric #3: α_{mag}

Whereas Q_z and Q_y derive from the critical linear wavelength of the MRI, the other diagnostics we have studied are more closely related to *nonlinear* development of the MHD turbulence. That is, they reflect how well a numerical calculation replicates macroscopic magnetic field properties related to the stress that are independent of discretization (i.e., convergence).

The first of the nonlinear diagnostics is the ratio of the Maxwell stress to the magnetic pressure, defined $\alpha_{mag} = -2B_R B_\phi / B^2$. Although turbulent Reynolds stress also contributes to angular momentum transport at a level roughly 1/4 of the Maxwell stress, it is difficult to quantify in global simulations, so we do not include it in our definition of α_{mag} . Even the earliest shearing box simulations (Hawley et al. 1995) found that this quantity was remarkably constant from simulation to simulation. More recently, Blackman et al. (2008) examined a large sample of published unstratified shearing box results and found that, quite generally, $\alpha\beta \propto \alpha_{mag}$ is roughly constant, where α is the traditional constant of proportionality between stress and (gas) pressure; the combination $\alpha\beta$ simply removes the gas pressure from consideration. Recomputing the results from Blackman et al. (2008) in terms of our definition of α_{mag} (i.e., without the Reynolds stress), we find that their derived values are more or less consistent with $\alpha_{mag} = 0.3$ – 0.4 as seen in the shearing box simulations reported here, except for the one with only 8 cells per H .

The values of α_{mag} presented in Table 1 are derived by taking the ratio of the Maxwell stress integrated over the central scale height to the similarly integrated magnetic pressure and then time-averaging; this is how α_{mag} has been determined in past shearing box simulations. Other averaging procedures, such as averaging the local ratio rather than taking the ratio of the averages, give values that are generally somewhat smaller. The data show that at a gross level, α_{mag} and α are correlated: a very low value of α_{mag} corresponds to a very low value of α . In the lowest resolution simulation discussed here, with only 8 cells per vertical scale height, $\alpha_{mag} = 0.08$. However, with an even modest improvement in resolution, both α and α_{mag} rise.

The value of α_{mag} is relatively constant because in MRI turbulence B_x and B_y are highly correlated. Both the background shear, which creates toroidal field out of radial, and the action of the MRI itself, which stretches out radial field as angular momentum is transferred between fluid elements, create this correlation. Time-averaging and volume-averaging over the central scale height, we find that the Pearson correlation coefficient $C(B_x, B_y)$ is -0.73, -0.70 and -0.67 for the 32, 64, and 128 zones per H Davis runs, and -0.28, -0.75, -0.73, and -0.71 for the 8 through 64 zones per H Simon runs. In other words, once one is past a resolution threshold (between 8 and 16 zones per scale height), the correlation rapidly

achieves a value $\simeq -0.7$. We have computed the correlation averaged over the (x, y) plane as a function of z . For $|z| < 2$ it is consistently ~ -0.7 , but approaches zero at higher altitudes. Two scale heights from the midplane is where the stress dies out (Simon et al. 2011; Guan & Gammie 2011).

We can probe a bit deeper into the nature of α_{mag} by studying its probability distribution over the set of grid cells. Figure 3 shows a time-averaged distribution function for α_{mag} for the region within 2 scale heights of the equator for each of the four Simon runs. The low resolution distribution function peaks around 0; there is very little net stress remaining within the decaying turbulence, even while the azimuthal field persists. As resolution increases, the distribution shifts to higher values, as does the mean value. On a zone-to-zone basis, α_{mag} is correlated with P_{mag} in the sense that where the field is particularly strong, the ratio of stress to magnetic pressure is also particularly high. In order of increasing resolution, the mean α_{mag} values are 0.057, 0.275, 0.346 and 0.380. Thus, improving resolution also leads to greater correlation between B_x and B_y , but the average α_{mag} saturates at ~ 0.4 .

Before leaving this topic, we note that the resolution-dependence of α_{mag} illustrates an important aspect of convergence-testing. If one compared its behavior in the 8 zone run with simulations having fewer cells per scale height, one might have concluded that α_{mag} is always $\ll 1$. In other words, low resolution simulations can be entirely blind to important effects, and convergence does not even begin until a resolution threshold is reached where that effect is at least minimally resolved.

3.4. Convergence metrics #4 and #5: $\langle B_x^2/B_y^2 \rangle$ and $\langle B_z^2/B_x^2 \rangle$

The α_{mag} parameter depends, in part, on the relative magnitude of the poloidal and toroidal magnetic field components and in part on the degree of correlation between the radial and toroidal components. As we have already seen in our discussion of the Q_z and Q_y diagnostics, the fidelity with which a given simulation follows the linear growth of these two field components can be different. The same may be true of their nonlinear characteristics.

To explore this question in a way that focuses on the separate components, independent of their correlation, we examined the time- and volume-averaged energy ratios $\langle B_x^2/B_y^2 \rangle$ and $\langle B_z^2/B_x^2 \rangle$ as functions of resolution. A relatively clear trend emerges from the former. Figure 4 shows the time history of this ratio for the simulations of Simon et al. (2011). It increases from < 0.01 to 0.15–0.18 from the worst to the best resolved models. Despite the substantial time variability, at every stage the curves in this figure are well-separated from each other, demonstrating a systematic increase of this parameter with resolution. When

one looks at the full ensemble of shearing box simulations, the dependence on resolution becomes even more striking (Fig. 5), with the value apparently leveling off near 0.2 at the highest resolution, when there are at least $\simeq 40$ cells per H . On the other hand there seems to be no general trend for the ratio of vertical to radial field energies, $\langle B_z^2/B_x^2 \rangle$; the values range from ~ 0.4 – 0.6 in these simulations.

Moreover, as we will discuss in greater detail later, there is a strong correlation between the Q values and $\langle B_x^2/B_y^2 \rangle$. The simulations achieving near-saturation values of $\langle B_x^2/B_y^2 \rangle$ (Simon64, Davis64, Davis128, and ShiDBLE) all have $Q_z \geq 10$ and $Q_y \geq 32$.

3.5. Summary: Stratified Shearing Box

In principle, a resolution study is directly applicable only to a set of simulations using the same numerical scheme on the same problem. Only after cross-comparison of parallel resolution studies can different algorithms be calibrated relative to one another. Previous comparisons between the *Athena* and *Zeus* simulations have indicated that *Athena* has lower turbulence decay rates for two-dimensional shearing sheet simulations compared to *Zeus* (Stone & Gardiner 2010; Stone 2009). Stone & Gardiner (2010) suggest that this is due to the use of third-order, rather than second-order spatial interpolation in *Athena* as well as the use of the HLLD-flux solver. In the studies gathered here, the contrast between *Zeus* and *Athena* is less obvious: the Shi et al. simulations and the Guan & Gammie (2011) *Zeus* models have diagnostic values comparable to equivalently resolved *Athena* runs.

Thus, from these simulations, we can conclude that for both *Athena* and *Zeus* simulations, stratified shearing boxes begin approaching convergence when resolution is around 40 zones per H . The quantitative changes that result in increasing the number grid zones beyond this point are noticeable, but small, compared to the decrease in zone size, i.e. convergence is occurring at a rate faster than linear in Δx . Adequate resolution requires both Q_z and Q_y to be sufficiently large, but an especially large value of one can somewhat compensate for a smaller value of the other. When $Q_y \gtrsim 20$, $Q_z \gtrsim 10$ suffices; however, when Q_y is smaller, $Q_z \gtrsim 15$ is required. A ratio of radial to toroidal magnetic energy greater than ≥ 0.15 and $\alpha_{mag} \simeq 0.3$ – 0.4 are signatures of well-developed MRI-driven magnetic turbulence.² The ratio of the vertical to radial magnetic field energy, on the other hand, shows no particular trend with respect to resolution.

²These values are obtained from shearing boxes without a net vertical field or applied resistivity or viscosity, as appropriate for the global simulations to be discussed here. Further work is required to characterize shearing box turbulence in the presence of net vertical field and non-ideal MHD effects

It is likely that the importance of Q_y stems from the essential role played by nonaxisymmetric processes in maintaining poloidal field energy and turbulence. Purely toroidal fields can support an active MRI-driven turbulence with relatively small vertical fields, but the vertical field MRI will necessarily generate toroidal field and nonaxisymmetric motions are essential to maintaining the poloidal field.

Moving in the direction of *reduced* resolution, we note that even if the characteristic MRI wavelength is unresolved (small Q) longer wavelengths will be unstable, albeit with smaller growth rates. Thus, lower resolution simulations can still have MRI-induced turbulence and stress, but at correspondingly reduced levels. Such a state will be indicated by smaller relative values of the convergence metrics. Of course, the results from the 8 zone per H simulation show that there is a resolution limit beyond which turbulence cannot be sustained.

4. Global Simulations

In this section we describe the results from a set of pseudo-Newtonian global disk simulations intended to investigate the influences of grid resolution and initial magnetic field strength and topology. What they show about progress toward numerical convergence will be discussed in the following section.

Our parameter study is centered around a fiducial model, designated twoloop-1000-mr, a simulation with initial $\beta = 1000$, a two-loop initial magnetic field, and grid M, the medium resolution grid. Using the same initial condition, we have explored the effects of both increasing and decreasing the grid resolution. To study the effects of different initial magnetic field configurations, we have also used the M grid for a simulation with a single dipolar loop initial condition and the same initial β , as well as both single and double dipolar loops with initial $\beta = 100$. The various models are listed in Table 2.

4.1. The Fiducial Run

The β value given for a torus is defined as the ratio of the total thermal to total magnetic pressure. Although the mean initial $\beta = 1000$, the β value at any given point within the torus varies. The minimum value is $\beta = 283$ and occurs along the radial field lines above and below the equator in the inner field loop; where the two loops meet at the pressure maximum, $\beta = 412$. For those regions of the torus where there is no magnetic field, β is nominally infinite. The initial resolution parameter Q_z has three maxima, each located where the vertical field crosses the equator. From inside out, these maxima are $Q_z = 15, 29,$

Table 1. Shearing Box Simulations

Reference	Zones/ H	Q_z	Q_y	B_x^2/B_y^2	B_z^2/B_x^2	β^{-1}	α_{mag}	α
Simon8 (unpub)	8	0.08	1.7	0.016	1.0	0.015	0.08	0.001
Simon16 (unpub)	16	2.0	13.	0.075	0.53	0.057	0.30	0.016
Simon32	32	5.7	27.	0.13	0.53	0.072	0.37	0.025
Simon64	64	11.	44.	0.17	0.53	0.056	0.40	0.020
Davis32	32	4.5	23.	0.12	0.41	0.078	0.33	0.020
Davis64	64	10.	40.	0.16	0.47	0.051	0.36	0.012
Davis128	128	26.	98.	0.18	0.50	0.053	0.36	0.018
ShiSTD	27	4.8	13.	0.10	0.65	0.075	0.27	0.020
ShiZ512	53	11.	13.	0.12	0.56	0.130	0.30	0.029
ShiDBLE	50	15.	32.	0.15	0.63	0.098	0.22	0.029
Guan std16	12.8	2.6	15.	0.07	0.58	0.035	0.28	0.013
Guan s16a	25.6	6.8	34.	0.12	0.58	0.057	0.32	0.023

Table 2. Global Simulations

Name	Grid	Type	Initial β	Duration (M)
twoloop-1000-mr	M	2-Loop	1000	66000
twoloop-100-mr	M	2-Loop	100	41000
twoloop-1000-lr	L	2-Loop	1000	41000
twoloop-1000-hr	R	2-Loop	1000	34000
twoloop-1000-mlp	PL	2-Loop	1000	40000
twoloop-1000-mhp	PH	2-Loop	1000	25000
oneloop-100-lr	L	Dipole 1-Loop	100	40000
oneloop-100-mr	M	Dipole 1-Loop	100	39000
oneloop-1000-mr	M	Dipole 1-Loop	1000	38000

and 20; the linear growth phase of the MRI should be well-resolved.

The fiducial model was run for $6.6 \times 10^4 M$ in time, corresponding to 54 orbits at the initial pressure maximum, and over 1000 orbits at the location of the ISCO, $R = 6M$. This evolution time is longer than previous global simulations, and permits an examination of the long term behavior of the accretion flow and MRI-driven turbulence at these resolutions. The evolution proceeds in several stages as identified by the evolution of the total magnetic energy (Fig. 6). First there is a period of exponential growth in the magnetic field. This is rather brief; by $t = 1000M$ (about 1.3 orbits at $R = 24M$), significant radial field has already grown to supplement the vertical field in the innermost part of the inner loop. This behavior is characteristic of the vertical field MRI. The total integrated radial field energy has doubled by this time; the vertical field energy doubles by $t = 1500M$. At first, the toroidal field grows as the MRI creates radial field and the background shear stretches radial field into toroidal; later azimuthal MRI modes also contribute to toroidal field amplification. By $t = 2000M$ the total toroidal field energy is 10 times as large as the total poloidal field energy, and significant accretion (mass flow off the inner radial boundary) has begun. Global field energy continues to rise until it peaks at $t \sim 8500M$. It then declines until $t = 1.5 \times 10^4 M$, after which the volume-integrated energies of the different magnetic field components vary slightly around a slowly declining trend line. We will refer to the period between $2000M$ and $1.5 \times 10^4 M$ as the “initial peak”; the remainder of the simulation we call the “quasi-steady state” period.

4.1.1. *Inflow equilibrium and the quasi-steady state*

Nearly every global disk simulation begins with a finite mass on the grid. Because accretion of some mass entails transfer of its angular momentum to other mass, part of the matter in the simulation must move outward as other mass moves inward. Consequently, at most only a portion of the disk can actually be in a state of inflow. At best, therefore, inflow equilibrium can be established only within some radius.

Having identified the largest radius within which inflow equilibrium can be sought, one might define inflow equilibrium to be a state in which the mass accretion rate is constant as a function of radius. The problem with this definition is that accretion is driven by the fundamentally chaotic process of MHD turbulence. The accretion rate at a specific radius must therefore always be highly variable in time. One solution is time-averaging; regions of inflow equilibrium would then be those ranges of radius over which the time-averaged accretion rate is constant.

A closely related procedure is to make use of the equation of mass conservation

$$\frac{\partial \Sigma}{\partial t} + \frac{\partial \dot{M}}{\partial R} = 0. \quad (14)$$

Here Σ is the surface mass density and \dot{M} the accretion rate integrated over the cylindrical surface at radius R . Clearly, wherever \dot{M} is independent of R , Σ is constant in time. Thus, one could also test $\Sigma(R, t)$ for time-steadiness across the radial range of interest. Equivalently, one could check that $M(< R, t) = \int^R dR' 2\pi R' \Sigma(R', t)$ is time-steady. This alternative has the conceptual advantage that it focuses squarely on the primary matter of interest: that the mass distribution in the disk does not change secularly over time. It also has the technical advantage that $\Sigma(R, t)$ changes more slowly than $\dot{M}(R, t)$, so results taken from simulation data are less subject to noise fluctuations.

Figure 7 shows $M(< R, t)$ for the fiducial run. The disk mass rises quickly during the first $10^4 M$ in time and then levels off. After that time, there is a slow secular diminution in the mass of the disk within $R = 20M$, but its characteristic timescale is quite long, $\simeq 5 \times 10^4 M$ at $R = 10M$, $\sim 8^4 M$ at $R = 20M$. Because the time to drain and replenish the region inside $R = 20M$ is $M/\dot{M} \simeq 1.5 \times 10^4 M$, this secular trend is quite slow compared to the characteristic mass equilibration time. Despite the overall steadiness of the radial mass profile, there are also shorter timescale fluctuations that become progressively larger in fractional terms at smaller radii, reaching $\sim 50\%$ at $R = 10M$. These reflect, of course, the continuing large amplitude fluctuations in the mass accretion rate both as a function of time and of radius. The slow diminution in inner disk mass reflects the declining trend in the magnetic energy, which leads to a parallel fall in the mass accretion rate.

Another way to test for inflow equilibrium is to compare the simulation time with an estimate of the characteristic inflow time. We can compute an average inflow velocity from simulation data by taking

$$\langle v_R(R) \rangle = \frac{\int \rho v_R R d\phi dz}{\int \rho R d\phi dz}. \quad (15)$$

These values are averaged over time to remove the ever-present fluctuations. The accretion time from radius R is then $t_{in}(R) = \int^R dR' / \langle v_R(R') \rangle$. Computing this for the fiducial run at $R = 20$ we obtain $1.2 \times 10^4 M$, consistent with the estimate above based on the average accretion rate and the disk mass interior to $R = 20M$.

How does this result compare to an estimate obtained from steady-state disk theory? In the steady-state limit the equation of angular momentum conservation is

$$W_{R\phi} = \frac{\dot{M}\Omega}{2\pi\Sigma} (1 - j_*/j) \quad (16)$$

where $W_{R\phi}$ is the vertically averaged $R\phi$ component of the stress tensor, and j and j_* are the specific angular momentum at R and the angular momentum accreted per unit mass. The j_* term determines the net flux of specific angular momentum; traditionally, it has been set to the angular momentum at the ISCO on the assumption that stresses cease there. Following Shakura & Sunyaev (1973), we write the vertically-integrated stress in units of the vertically-integrated pressure and assume there is a single temperature throughout the flow; i.e., we set $W_{R\phi} = \alpha \Sigma c_s^2$. With those assumptions, we obtain for the steady-state mean infall velocity

$$\langle v_R \rangle_{SS} = \frac{\dot{M}}{2\pi R \Sigma} = \frac{\alpha c_s^2}{R \Omega} (1 - j_*/j)^{-1}. \quad (17)$$

Agreement between the inflow velocities from (15) and (17) would indicate that the observed mass accretion is in approximate steady state at a rate consistent with the angular momentum transport produced by the observed stress.

We test this for the fiducial run for a time average over $10^4 M$ beginning at $t = 4 \times 10^4 M$. We compute a vertically and time-averaged Maxwell stress, pressure, and density to obtain α and c_s^2 . The average value of α thus obtained for the Maxwell stress is 0.017. To account for the Reynolds stress (not directly measured in global simulations), we increase the value of α in (17) by 25%, a value consistent with results from shearing box simulations. The velocity derived from the steady state disk model (with $j_* = j_{ISCO}$) and the velocity obtained directly from the accretion rate and the mass are compared in Figure 8. The agreement is good out to just beyond $30M$. This match is consistent with the range over which the time-averaged \dot{M} is constant with radius, the computed t_{in} at $30M$ which is $4.5 \times 10^4 M$, and our estimates based on the evolution of $M(< R, t)$ as described above. The two curves deviate outside of $R \sim 32M$ because there the infall time begins to exceed the simulation time. At small radius the curves deviate because the stress does not go to zero at the ISCO; reducing j_* to $0.985 j_{ISCO}$ brings the curves into line right down to the ISCO.

4.1.2. Comparison with shearing box results

The initial transient and quasi-steady periods are seen in both global and shearing box simulations. Figure 9 plots the total magnetic field energy, normalized to its peak value, as a function of time in units of orbits at the initial pressure maximum. Overlaid on this is the evolution of the total magnetic field energy in the stratified shearing box simulation with 16 zones per H , again normalized to the initial peak value. Because the early evolution of the global simulation is relatively local, dominated by MRI growth in the confined region where its growth rate is greatest (i.e., the inner rings of the initial torus), it is perhaps not surprising that the initial evolutions are similar. More interesting, perhaps, is the similarity between

the two models during the subsequent quasi-steady state phase. Between 20–50 orbits in each run, the ratios of the total average radial to toroidal magnetic field energy, $\langle B_R^2/B_\phi^2 \rangle$, are 0.068 and 0.070 for the shearing box and the fiducial model, respectively. This similarity suggests that the effective resolution in the fiducial global simulation, at 14–60 zones per H depending on radial location, is comparable to the 16 zones per H used in the shearing box. A comparison with Fig. 2 shows that higher resolution shearing box simulations have a smaller decline in stress immediately after the initial peak. The 16 zone shearing box simulation, however, sees a regrowth of field energy beyond orbit 50 that is not seen in the global simulation. The reason for this is uncertain. It could be due to the better azimuthal resolution in the shearing box, possibly by better capturing a (nonaxisymmetric) dynamo process. Another possibility is that the observed field regrowth is due to other properties associated with the shearing box, e.g., restricted box size, shearing-periodic boundaries, and overall symmetry.

Among the differences between shearing box and global simulations is the latter’s large dynamic range in Ω , which is important because the MRI e -folds at a rate $\sim \Omega$. As a result, a single spatially-averaged value is not very useful for comparison with shearing boxes. Instead, we show figures of the principal diagnostic quantities as a function of radius, averaged in time and azimuthally- and vertically-averaged weighted by density (Figs. 10 and 11). In each case, the averaging interval was chosen to be the longest time-span covering the quasi-steady epoch for all simulations shown in a given figure; consequently, the averaging periods for the different figures are different. Likewise in each case, the radial range was restricted to the region defined as the “inner disk,” $6M < R < 20M$ in order to focus attention on the portion of the simulation most closely resembling a statistically time-steady accretion flow.

Data from the fiducial run appear in both of these figures. Its density-weighted $\langle Q_z \rangle$ drops steadily inward, from $\simeq 8$ at $R = 20M$ to < 2 at $R = 6M$. By contrast, its $\langle Q_\phi \rangle$ value varies only slightly with radius, remaining near $\simeq 8$ – 10 throughout the inner disk. Both behaviors—the strong dependence of $\langle Q_z \rangle$ on radius and the near-constancy in radius of $\langle Q_\phi \rangle$ —are characteristic of all the simulations. $\langle B_R^2/B_\phi^2 \rangle$ displays a radial profile very similar to that of $\langle Q_z \rangle$, falling from $\simeq 0.08$ in the outer part of the inner disk to $\lesssim 0.04$ just outside the ISCO at $R = 6M$.

Thus, even with a poloidal cell-count of 256×288 , the fiducial run is, at best, marginally resolved according to both the Q_z and Q_ϕ criteria. There is adequate resolution to describe linear MRI growth of poloidal perturbations only near $R = 20M$; nowhere in the inner disk is it well enough resolved to describe poloidal nonlinear behavior properly. The azimuthal resolution is no better: $\langle Q_\phi \rangle$ never reaches the $\simeq 20$ level indicated by shearing box simulations. Similarly, the value of the nonlinear criterion $\langle B_R^2/B_\phi^2 \rangle$ is at most only about half

what the shearing box simulations suggest is characteristic of well-resolved turbulence. It is near to the value seen in the marginally resolved 16 zones per H shearing box.

The radial gradient in $\langle Q_z \rangle$ is an illustration of how grid-design can interact with physics. The definition of this quantity is $2\pi|v_{Az}|/(\Omega\Delta z)$. In the cylindrical coordinates used here, Δz is independent of radius. Consequently, $Q_z \propto v_{Az}(R)R^{3/2}$; unless v_{Az} rises rapidly inward, poloidal resolution quality falls toward small radius. Here the average v_{Az} goes roughly like $R^{-1/2}$ in the inner disk so $\langle Q_z \rangle \propto R$. By contrast, $Q_\phi \propto v_{A\phi}R^{1/2}/\Delta\phi$, leading to its much weaker dependence on R . The end-result of these different dependencies on radius is that, unless Q_z is very large at larger radii, the linear growth rate of axisymmetric MRI modes will be reduced in the inner disk even while non-axisymmetric modes continue to grow at their correct (albeit slower) rate.

The radial gradient in $\langle Q_z \rangle$ also provides a finely-sampled measure of convergence properties. At each radial cell, these global simulations sample a different effective resolution. As we will discuss in § 5, this effect allows us a much more quantitative measurement of the convergence rate than we would otherwise be able to obtain.

4.2. Different grid resolutions

Table 3 lists time- and volume-averaged values for various parameters, both diagnostic and physical, as well as the time-averaged accretion rate through the inner R boundary as a fraction of the initial torus mass. The time averages are taken over the steady state period for each simulation; the volume averages are limited to the inner disk body. For those parameters with potentially significant radial gradients, a range of values is given: the first number refers to the value at $R = 6M$, the second to $R = 20M$. The scale height H is defined by a time- and density-weighted mean of $\sqrt{2}c_s/\Omega$. In these simulations, in which total energy is not conserved, c_s scales with radius roughly $\propto R^{-1/2}$, so that H is approximately $\propto R$. In most cases, α_{mag} increases outward, but simulation twoloop-1000-hr is an exception: in that case, α_{mag} decreases slightly toward larger radius.

4.2.1. Azimuthal Resolution

We next consider how the results seen with the fiducial model change as the resolution is altered. We begin with a study of the ϕ resolution (Fig. 11). Model twoloop-1000-mlp uses grid PL, which decreases the number of ϕ zones to 32 while gaining a modest increase in radial resolution due to bringing in the outer boundary somewhat. Twoloop-1000-mhp uses

grid PH, which is the same as the M grid, but with an increase in the number of ϕ zones to 128. As the orbital speed generally sets the Courant limit in these simulations, this high- ϕ resolution model is more costly to evolve.

Figure 12 shows the evolution of the total poloidal magnetic energy as a function of time for the three runs. For the 32 zone run, exponential growth ends earlier compared to the other simulations, with a more gradual climb to a peak value. The 128 zone run leaves the rapid growth stage earlier than the 64 zone run, but when it levels off after declining from its magnetic energy peak, it does so at a higher level. Thus, the sustained field energies after the initial peak are clearly separated by resolution.

As shown in Figure 11c, for $R \gtrsim 12\text{--}15M$, $\langle Q_\phi \rangle$ increases by roughly a factor of 2 for each factor of 2 improvement in resolution. Notably, however, both poloidal indicators, $\langle Q_z \rangle$ and $\langle B_R^2/B_\phi^2 \rangle$, also respond positively to improvement in toroidal resolution at larger radii within the inner disk. Like $\langle Q_\phi \rangle$, the response to improved resolution is even stronger between the M and PH grids than between PL and M. In other words, *improved azimuthal resolution leads to stronger poloidal field, even in the absence of improved poloidal resolution*, and this effect strengthens with finer azimuthal resolution.

4.2.2. Poloidal Resolution

Figures 13 and 10 show the diagnostics for one-loop and two-loop initial field configurations with a range of resolutions. In the one-loop cases, a factor of 2 improvement in poloidal resolution yields an equal factor in $\langle B_R^2/B_\phi^2 \rangle$ and a factor of 3 improvement in $\langle Q_z \rangle$. Moreover, even with a grid of $256 \times 64 \times 288$ zones, these simulations remain unresolved. The best $\langle Q_z \rangle$ was only $\simeq 10$, while it fell below 6 inside $R \simeq 10$; $\langle B_R^2/B_\phi^2 \rangle$ hovered around 0.1 outside $R \simeq 15M$, falling to 0.06–0.07 near the ISCO, whereas the shearing box simulations indicate a converged value of almost 0.2.

Within the two-loop series of simulations, we find that the move from the L poloidal grid to the M yielded the same level of improvement as in the one-loop case: a factor of 2 in $\langle B_R^2/B_\phi^2 \rangle$ and a factor of 3 in $\langle Q_z \rangle$. However, progress stalls when only the radial zone size is reduced, as in the R grid. Outside $R \simeq 10\text{--}12$, the finer radial resolution actually led to a deterioration in both $\langle B_R^2/B_\phi^2 \rangle$ and $\langle Q_z \rangle$. We speculate that this may be due to the highly-elongated cells created in this grid by its finer radial resolution. In contrast to the M grid, in which $R\Delta\phi/\Delta R \simeq 0.4\text{--}1.4$, that ratio is 4–6 in the R grid, increasing toward larger radii.

Although not illustrated in the figures, much the same can be said about the effect of

Table 3. Resolution Comparisons

Name	R, ϕ, z zones	\dot{M}	α_{mag}	Q_z	Q_ϕ	B_R^2/B_ϕ^2	B_z^2/B_ϕ^2	Cells per H
twoloop-1000-mr	$256 \times 64 \times 288$	2.71×10^{-6}	0.24–0.33	1.6–7.5	7.9–10.	0.040–0.077	0.0088–0.018	11–60
twoloop-100-mr	$256 \times 64 \times 288$	2.51×10^{-6}	0.29–0.37	3.0–9.0	12.–11.	0.054–0.092	0.012–0.023	14–65
twoloop-1000-mlp	$256 \times 32 \times 288$	1.99×10^{-6}	0.25–0.24	4.2–4.5	8.5–6.0	0.059–0.046	0.016–0.012	8–49
twoloop-1000-mhp	$256 \times 128 \times 288$	4.40×10^{-6}	0.23–0.41	2.1–11.	22.–22.	0.045–0.13	0.0079–0.035	13–57
twoloop-1000-lr	$128 \times 64 \times 144$	0.94×10^{-6}	0.095–0.25	0.46–2.3	5.7–9.4	0.019–0.050	0.0055–0.0081	8–30
twoloop-1000-hr	$816 \times 64 \times 288$	1.89×10^{-6}	0.31–0.29	3.8–4.9	13.–11.	0.064–0.057	0.021–0.022	10–46
oneloop-1000-mr	$256 \times 64 \times 288$	3.85×10^{-6}	0.29–0.35	2.8–9.1	12.–11.	0.059–0.086	0.012–0.024	14–60
oneloop-100-lr	$128 \times 64 \times 144$	1.43×10^{-6}	0.13–0.29	0.42–3.3	5.6–12.	0.017–0.065	0.0053–0.013	9–36
oneloop-100-mr	$256 \times 64 \times 288$	7.92×10^{-6}	0.30–0.38	3.0–10.	13.–12.	0.063–0.10	0.010–0.033	13–76

resolution on α_{mag} . When the magnetic geometry is held fixed and only resolution changes, finer resolution in both the poloidal and azimuthal grid lead to larger values of α_{mag} .

Overall, it appears that improving radial resolution without also improving either vertical or (perhaps especially) azimuthal resolution does not yield significant progress toward convergence. As we have seen, the linear indicators (Q_z and Q_ϕ) do not grow (if anything, they fell in this case), nor do nonlinear indicators such as $\langle B_R^2/B_\phi^2 \rangle$ improve.

4.3. Different initial magnetic fields

All simulations must begin from some particular magnetic field. The problem, of course, is that we can only guess at what might actually occur in Nature. We have no way to say what geometric structure it might have, yet numerous variations are imaginable. The field may or may not have net flux; even if it has no net flux, it may be predominantly toroidal or poloidal; and numerous sorts of poloidal configurations are possible. Even granted the field geometry, we must still specify its initial strength; so long as it corresponds to a plasma $\beta \gg 1$, we have no guidance in this respect either. The most we can hope for is that in the end the resulting steady state accretion flow is independent of our arbitrary choices.

We begin with the question of sensitivity to initial field strength with a comparison of oneloop-100-mr and oneloop-1000-mr. Stronger fields, of course, will have an initial advantage of larger Q values at a given resolution. In the quasi-steady state period, as shown by Figure 13, a factor of 10 in initial magnetic field pressure makes a consistent, but very small difference: the stronger initial field in general has larger values of the diagnostics, but only by $\sim 10\%$. There is a greater contrast between twoloop-100-mr and twoloop-1000-mr, generally $\simeq 20\text{--}30\%$ and in some places larger. Like the one-loop case, the simulation with the initially stronger field retains that advantage.

The main effect of a stronger initial field is in the initial evolution; it creates stronger accretion early on and fills the inner disk with matter at a faster rate. This happens for two reasons, neither of which has much long-term effect. The first is that the stresses driving the initial inflow are not created by correlated MHD turbulence, but by the shear that transforms the initial poloidal field into toroidal. The second is that in the initial state, $\langle Q_z \rangle$ is smaller if the field is weaker, depressing the linear MRI growth rate in some locations. In the end how the mass distribution reaches its steady-state is not important, so long as one evolves long enough to reach the steady-state.

We next turn to the question of field geometry. Beckwith et al. (2008a) demonstrated that the magnitude of the axial funnel field attached to the black hole, capable of powering

a jet when the black hole spins, depends strongly on whether the vertical component of the initial magnetic field in the simulation has a consistent sense over a wide span of radii—the jet luminosity is substantial only when it does. They also showed that the accretion flows in the cases they considered depended much less on the field structure, although the stress levels and accretion rates are noticeably lower when the initial field is purely toroidal. Here we take a closer look at the accretion flows associated with two specific initial field configurations: one initial dipole loop versus two.

The first point is that the two-loop configuration does not persist throughout the simulation. Distinguishing the loops by their sign of A_ϕ , the azimuthal component of the vector potential, we find that in the fiducial model the disk inside $R = 20M$ is effectively dominated by the inner loop until $t \sim 10^4M$. By the end of that period, much of the inner loop’s flux has been accreted through the inner boundary, and the remainder has risen to high altitude and left the disk proper. For the next $\sim 10^4M$, the main body of the disk is entirely dominated by the outer loop. Between $\sim 2.2 \times 10^4M$ and $\sim 3.2 \times 10^4M$, enough inner loop flux has settled into the disk that it is very mixed. During this period, there is significant reconnection between oppositely directed field loops. For the remainder of the simulation (until $t = 6.6 \times 10^4M$), the disk is once again dominated by poloidal field loops having the sense of the outer of the two initial loops. In other words, with the exception of an episode that lasts only $\sim 1/6$ of the simulation, there is little to distinguish the poloidal field geometry in the inner disk of a two-loop simulation from one that begin with only a single set of poloidal loops. In both cases, there is a consistent sign of A_ϕ (i.e., consistent sense of field circulation) in the inner disk, but with a highly complex structure (the more fully-developed the turbulence, the more complex, of course).

Nonetheless, our time-averaged diagnostics do show interesting contrasts between the one-loop and two-loop results (Figs. 13 and 10). At low-resolution, the $\langle Q_z \rangle$ diagnostic improves by $\sim 50\%$ from two-loop to one-loop at all radii. At medium-resolution, $\langle Q_z \rangle$ in the one-loop case is only about 10% greater in the disk body (e.g., $R = 20M$) than for the two-loop case, but that advantage widens toward smaller radii, rising to almost a factor of 2 by $R = 10M$. Very similar contrasts are found for $\langle B_R^2/B_\phi^2 \rangle$. Although the magnitude of the change is smaller, the trend is the same for α_{mag} .

One might reasonably ask why these contrasts occur, given our assertion that the inner disk magnetic field at any single time generally has a uniform sign of A_ϕ . A clue comes from looking at their time-variation. During the period $1\text{--}2 \times 10^4M$, the diagnostic quantities in twoloop-1000-mr are, in fact, very similar to those of oneloop-1000-mr. Their decline at small radii takes place only after 2×10^4M , the time when oppositely-directed field loops reenter the disk. That re-entry is extremely irregular and creates gradients in A_ϕ on very

short lengthscales. For the same gridscale, the larger amount of short lengthscale fluctuation power leads to a faster numerical reconnection rate. This, in turn, weakens the magnetic field to the point that the MRI is unable to rebuild the field strength, even after the period of enhanced reconnection is over. Throughout this later period Q_z is only $\simeq 2\text{--}8$, insufficient to drive the MRI at its full rate.

Thus, the two-loop initial condition creates—through a rather recondite mechanism—considerable short length-scale power that requires a finer resolution grid to treat properly. In principle, a weakened magnetic field (and therefore smaller values of $\langle Q_z \rangle$ and $\langle Q_\phi \rangle$ for a fixed gridscale) might be a physical consequence. However, there is clear evidence that this really is a resolution effect. As we have just pointed out, the prevailing Q_z after the strong reconnection epoch is inadequate to drive linear MRI growth, much less support nonlinear poloidal dynamics. The low value of $\langle B_R^2/B_\phi^2 \rangle$ further supports our conclusion that the turbulence is less than fully-developed at late times in the two-loop simulations.

5. Interpretation

The principal goal of this paper is to develop from highly resolved shearing box models a set of diagnostics that can be applied to gauge how well global simulations represent the quasi-stationary behavior of a disk obeying the same physics as in the simulation. In this section we will discuss how to use the diagnostics we have identified, making use of their application to the simulations described in the previous section.

One might have supposed that the most natural quantity to study as a gauge of progress toward convergence is the stress, the physical quantity of central interest to the entire subject. However, there are several good reasons *not* to use it. The first is that it is not dimensionless. A similar statement can be made about the accretion rate. It can be useful to compare quantities such as stress and accretion rate between a set of simulations with the same initial conditions, but a comparison of any dimensional value across different simulations would need calibration in terms of other quantities.

The stress is often quoted in units of the gas pressure, giving it an apparently “natural” dimensionless form, but it is not at all clear that this form is appropriate. We do not know whether the pressure is the only variable influencing the stress, or whether the dependence is linear. Fluctuation timing correlations (Hirose et al. 2009) suggest that the relationship is more complicated than commonly thought. In addition, even if stress were dependent only on the pressure and exactly proportional to it, the great majority of accretion simulations treat thermodynamics with very crude approximations, making the value of the pressure

both questionable and difficult to compare from one simulation to the next. For all these reasons, therefore, we prefer to use diagnostics that are dimensionless ratios of quantities referring only to magnetic properties.

5.1. Relationship between the different diagnostics

Each of our diagnostics has a slightly different standing. $\langle Q_z \rangle$ and $\langle Q_\phi \rangle$, for example, depend directly on cell sizes in the grid and can be meaningfully evaluated on the initial data whenever it includes either vertical magnetic field (for $\langle Q_z \rangle$) or toroidal field (for $\langle Q_\phi \rangle$). In that sense, they are predictive measures of the ability of the simulation to describe accurately the linear growth of, respectively, the axisymmetric and non-axisymmetric branches of the MRI. At the same time, however, both are also simulation products because their values change as the field strength evolves; in that sense, they also serve as diagnostics for the fully developed MRI-driven turbulence.

The quantity $\langle B_R^2/B_\phi^2 \rangle$ has little significance in the initial state; it is simply a function of the initial magnetic field. It is not even defined if the initial field is entirely poloidal. Thus, it is purely a product of the simulation; the same is true of α_{mag} .

The definitions of the Q parameters have an explicit dependence on grid size; their values can never converge with increased resolution. In contrast, $\langle B_R^2/B_\phi^2 \rangle$ and α_{mag} measure physical quantities and do not have an explicit dependence on resolution in their definitions. In principle, they could be measured in a laboratory experiment. Thus, they signal progress of the simulation toward achieving the true physical state of the MHD turbulence, no matter what resolution or algorithm has been used.

Despite these contrasts in status, there is a tight relationship between these different diagnostics of resolution quality. This relationship is illustrated in Figure 14. Although the filled circles in this figure are drawn from 11 different times at all radial cells in the inner disk in each of 3 different simulations (twoloop-1000-lr, twoloop-1000-mr, and twoloop-1000-mhp) that differ in both poloidal and azimuthal gridding, they closely follow a single track: $\langle B_R^2/B_\phi^2 \rangle \simeq 0.01 \langle Q_z \rangle^{0.65}$ for $\langle Q_z \rangle \lesssim 10\text{--}12$, flattening out at larger $\langle Q_z \rangle$, where it rises slowly to almost 0.2. The crosses, squares, and diamond represent the time-averaged values in the midplane region of the different stratified shearing box simulations; the different symbols distinguish different ranges of $\langle Q_y \rangle$ (the crosses have similar $\langle Q_y \rangle$ to $\langle Q_\phi \rangle$ in the global simulations; the others have larger $\langle Q_y \rangle$). The shearing box simulations with $\langle Q_y \rangle$ similar to the $\langle Q_\phi \rangle$ values of the global simulations lie very close to the track defined by the global simulations. Consonant with our finding that better azimuthal resolution also strengthens

poloidal field, the shearing box results with larger $\langle Q_y \rangle$ lie somewhat above the track; that is, larger $\langle Q_y \rangle$ can compensate to a certain degree for smaller $\langle Q_z \rangle$. Taken as a whole, this figure confirms that for global simulations as well as for shearing boxes, convergence in $\langle B_R^2/B_\phi^2 \rangle$ does not begin until $\langle Q_z \rangle \gtrsim 10$ –15 for typical global simulation azimuthal resolution (i.e., $\langle Q_\phi \rangle \simeq 10$); larger $\langle Q_y \rangle$ ($\gtrsim 25$) can relax this requirement slightly.

5.2. Importance of y/ϕ -resolution

In most of the MRI literature hitherto, discussion of resolution criteria has generally focused on poloidal gridding, particularly the Q_z criterion established by Sano et al. (2004). Less attention has been paid to the ϕ resolution. It is generally understood that in multi-dimensional simulations one should avoid cell aspect ratios that are too far from unity. Accuracy in directionally split algorithms requires that the truncation errors in the different spatial directions not be too different. In any case, if the truncation error in one spatial direction remains large due to a lack of resolution, improvements in resolution in other dimensions will be of limited value due to the dominance of that error.

In the context of disk dynamics, including shearing box simulations, experience suggests that even though it is best for $\Delta R/\Delta z \sim 1$, ratios $R\Delta\phi/\Delta R$ as large as ~ 4 are acceptable because orbital shear tends to stretch out features in the azimuthal direction. Our findings here suggest that larger ratios, such as are found in twoloop-beta1000-hr, tend to weaken the development of MHD turbulence even though the unfavorable ratio was created by improved radial resolution.

To our knowledge, the comparisons presented here are the first to underline the importance of adequate $\langle Q_\phi \rangle$. Our analysis indicates that sufficiently large $\langle Q_\phi \rangle$ is necessary for the proper development of poloidal properties such as $\langle B_R^2/B_\phi^2 \rangle$ and maintenance of a large $\langle Q_z \rangle$. This is, perhaps, not so surprising as it is well-understood that non-axisymmetric motions are essential for maintaining poloidal field in the face of dissipation (the “anti-dynamo” theorem). Even the earliest stratified shearing box simulations found evidence for a dynamo process (Brandenburg et al. 1995), and recent simulations have shown explicitly that magnetic field evolution can be empirically modeled with a simple α – Ω dynamo equation (Guan & Gammie 2011; Simon et al. 2011). Although we have yet to develop a detailed understanding of the mechanism by which the MRI creates the α -effect that generates poloidal field from toroidal, it clearly requires adequate resolution to be effective. Future simulations should therefore be graded on their values of $\langle Q_\phi \rangle$ as well as $\langle Q_z \rangle$.

Finally, one should bear in mind that ϕ resolution might well be much more important

in global simulations compared to local. The shearing box is in a local co-rotating frame whereas the global simulation must deal with the full orbital velocity. If one assumes that the numerical dissipation level in a code is proportional to a diffusion coefficient, e.g., $\Delta x^2/\Delta t$, then the diffusion will be roughly proportional to the fastest velocity times Δx because $\Delta t \sim v_*/\Delta x$, where v_* is that fastest velocity. For a global simulation, the orbital velocity is $R\Omega \propto (R/H)c_s$. Because for a shearing box the fastest velocity is $\leq c_s$, one might well require R/H more grid zones in the ϕ direction compared to a shearing box in order to have similarly low levels of diffusion. For global thin disk simulations this requirement is particularly problematic.

5.3. Connection with stress

It would seem natural that stronger magnetic fields would lead to larger stress. In fact, the correspondence between the hierarchy we see in our diagnostics ($\langle Q_z \rangle$, $\langle Q_\phi \rangle$, $\langle B_R^2/B_\phi^2 \rangle$, α_{mag}) is reproduced closely in stress levels. Figure 15 plots the stress as a function of radius and can be compared with the previous figures showing diagnostic quantities versus radius. As the diagnostics indicate better resolution, the stress rises. Moreover, when poloidal resolution is improved and the general level of stress rises, so does the ratio between stress near the ISCO and stress in the disk body. Although not illustrated in the figure, this trend also applies to the radial stress profile at particular times during an individual simulation. Higher stress levels at larger radius generally correspond to higher stress throughout the flow, even if the stress and the Q values decrease moving in. The ISCO-region stress appears even more sensitive to the prevailing stress than the stress in other regions of the inner disk.

Because even relatively low resolution simulations nevertheless show some stress due to MRI-turbulence, the mere presence of stress and accretion are not themselves indicative of convergence in any sense. Weak fields remain unstable at longer (better resolved) wavelengths, but at greatly reduced growth rates. As we have tried to make clear, not even the best-resolved global simulations shown here appear to be near the diagnostic levels identified as adequate in the shearing box models. Even if some regions satisfy the resolution criteria, their variation with radius means they are not satisfied *globally*. We expect that still better-resolved simulations can be expected to show both higher stress levels overall, and a greater ratio of ISCO-region stress to stress in the disk body.

5.4. Effects of the initial magnetic configuration

Because the MRI grows exponentially when the initial field is weak ($\beta \gg 1$), it has long been hoped that the saturated state of this instability would be independent of the initial field intensity. The stress in unstratified shearing box simulations depends on the net value of the initial field (e.g., Hawley et al. 1995; Sano et al. 2004), but this probably reflects the constraints imposed by the shearing box boundary conditions, which preserve net magnetic flux. In less-constrained global simulations one might expect the field to evolve to some self-consistent average magnetic energy with β somewhere below equipartition, independent of the field’s initial strength, even though local regions may have persistent net vertical flux (Sorathia et al. 2010). Although we have not made extensive comparisons of simulations with different initial values of β , those we have examined are consistent with this hope. In the quasi-steady state period there are only modest differences between our 1- and 2-loop simulations with initial $\beta = 100$ and $\beta = 1000$, for example.

Field geometry can matter, however, in the way in which it interacts with grid resolution. Intuitively, one might suppose that a correct discretized description of any field requires a grid with a characteristic scale significantly smaller than the field’s characteristic lengthscale of variation. Applying that argument in the present context suggests that initial fields with more small-scale structure require finer grids to describe accurately. The contrast between our results for the 1-loop and 2-loop simulations supports this suggestion, although, as we have explained, the specific way in which the small-scale structure is created is rather more complicated than one might have guessed. Introducing oppositely-directed field-loops creates more opportunities for reconnection, and this rate is enhanced by coarse resolution. Because the ability of a given grid to support field growth through MRI stirring depends on the field strength itself when the resolution is marginal, excessive numerical reconnection can lead to a long-term suppression of the field intensity.

This has implications for comparing physically significant quantities such as accretion rate or stress in simulations with differing magnetic field geometry. Without clear proof of convergence, the contrast between them as simulated with the same grid is as likely to be due to a contrast in *effective* resolution as it is to be due to a contrast in the real physical behavior of the different systems.

5.5. Inflow equilibrium

In shearing boxes one measures the properties of the MHD turbulence after many tens of orbits, when a quasi-steady state is clearly established. In global simulations one looks for

inflow equilibrium, a desirable property because it is the primary prerequisite for achieving a statistically stationary state. Any other state could, in principle, exhibit properties resulting more from transients due to arbitrary choices in the initial conditions than to the intrinsic physics of the system. Its meaning, however, requires precise specification in order to test how well a simulation matches this condition. The key question is how long to evolve a global simulation in order to reach a reasonable approximation to equilibrium.

We have used several procedures for determining inflow equilibrium. One is to measure $M(< R, t)$, the mass interior to radius R as a function of time. A related procedure is to compute the characteristic inflow time from accretion rate and mass distribution, M/\dot{M} , and the average inflow velocity $\langle v_R \rangle$. This, in turn, can be compared to the inflow velocity derived using the time-averaged stress and steady state disk theory. Agreement indicates that the observed mass accretion rate is consistent with the observed angular momentum transport. For the fiducial run we find that all these measures give comparable results and show that the disk inside of $R \sim 30M$ is in inflow equilibrium.

It is worth noting that Penna et al. (2010) proposed an alternative definition of inflow equilibrium time at radius R , specifically $2R/\langle v_R \rangle$ (rather than $\int dR/\langle v_R \rangle$), solely in terms of a general scaling argument. Because the magnitude of $\langle v_R \rangle$ increases rapidly inward, there is a large difference between the local infall estimate R/v_R and the actual integrated infall time. The Penna et al. value of the inflow equilibrium time is, for example, a factor of 7 larger at $R = 20M$ than the actual inflow time $\int dR/\langle v_R \rangle$ in the fiducial run. In fact, the inflow time estimated from $2R/\langle v_R \rangle$ at the initial torus pressure maximum exceeds the time required to accrete the *entire* initial torus at the observed \dot{M} .

More generally, although an order of magnitude scaling argument may provide a rough rule-of-thumb for estimating the equilibration time, it does *not* provide a rigorous criterion. Only observed properties of the inflow can be used to test whether it is in equilibrium. After all, how a disk achieves a quasi-steady state is irrelevant; if the initial condition (miraculously!) agreed identically with the steady-state mass profile, it would be as good an equilibrium as one achieved after long computation. In fact, a commonly-used initial condition (one in which the magnetic field is dominated by large dipole loops; our 1-loop simulations are examples) behaves roughly in this way. Large turbulent magnetic stresses develop early in the simulation at the inner edge of the initial torus, pulling mass into the inner disk far more quickly than would happen at later, more representative, stages of evolution. Once the inner disk is filled with matter, however, it evolves toward an appropriate time-steady condition. The large transient magnetic stresses are simply a “jump-start” that allows a more rapid approach to the steady-state.

As a final comment on this topic, we also wish to emphasize that achievement of in-

flow equilibrium does *not*, on its own, signal numerical convergence. In almost all of the global simulations we report here, the late-time state was one of approximate steady-state in terms of mass inflow within the inner disk, yet for none of them would we claim numerical convergence.

5.6. Resolution and Numerical Dissipation Rate

In simulations such as these, in which there is no explicit resistivity or shear viscosity, dissipation of turbulence occurs entirely due to gridscale discretization error (and any artificial viscosity). This is true regardless of whether one uses an internal energy algorithm such as *Zeus* or an energy conservative scheme such as *Athena*. It follows that the numerical dissipation rate is affected by cell-size. Because short lengthscale dissipation is the primary means by which magnetic (and kinetic) energy is lost, the saturation strength of the turbulence depends directly on this dissipation rate. To understand how resolution affects the amplitude of the magnetic field therefore requires a closer consideration of gridscale losses.

In the shearing box simulations of Hirose et al. (2006), the local rate of this sort of dissipation scales $\propto |\mathbf{J}|^{1.1}$ for electric current density \mathbf{J} . In other words, by Ampère’s Law, numerical dissipation is roughly proportional to the cell-by-cell contrast in $|\mathbf{B}|$. If the local scaling were *exactly* proportional to $|\mathbf{J}|$, then the box-integrated dissipation would be likewise proportional to the box-integrated $|\mathbf{J}|$. However, if there is any departure from linearity, it is necessary to be more careful in regard to the distribution function of current density over the box.

The best data we have available for this purpose comes from the simulations of Shi et al. because their code explicitly tracked the several different kinds of gridscale dissipation. With remarkably little scatter, this data shows that the box-integrated magnetic dissipation rate $Q_{\text{tot}} \propto J_{\text{tot}}^{2.5}$, where J_{tot} is the box-integrated current density. Because this is *numerical* dissipation, not physical, it must depend on the cell-to-cell contrast in \mathbf{B} , rather than on the actual current. Its most appropriate dimensional form is therefore

$$Q_{\text{tot}} = q \frac{\langle \delta B_{\text{grid}} \rangle^{5/2}}{\Delta t} p^{-1/4}, \quad (18)$$

where q is a number of order unity, Δt is the time-step in the simulation, and p is the pressure. We evaluate $\langle \delta B_{\text{grid}} \rangle$ as $\langle |\nabla' \times \mathbf{B}| \rangle$, where ∇' denotes a **curl** operator defined with respect to cell-index rather than distance. As resolution improves, one would expect the cell-to-cell contrast to diminish, reducing Q_{tot} . However, there are countervailing effects: in turbulence, new short lengthscale power can readily be generated by nonlinear transfer from longer wavelengths; and the time-step Δt also decreases.

In fact, the time-step Δt depends on spatial resolution in two ways: $\Delta t = \Delta x/c_s$, and c_s depends on resolution because Shi et al. found that over their range of resolutions the total, i.e., gas plus radiation, pressure had not yet converged; it scaled roughly $\propto (\Delta x)^k$, with $k \simeq -0.45$. At fixed surface density, hydrostatic balance implies that $c_s \propto p$, so $\Delta t \propto (\Delta x)^{1-k}$. Thus, we expect that the overall resolution scaling of Q_{tot} should be $\propto \langle \delta B_{\text{grid}} \rangle^{5/2} (\Delta x)^{-4/3}$. Comparing the Q_{tot} versus $\langle \delta B_{\text{grid}} \rangle$ relations found in the Shi et al. simulations, we find that the actual exponent of Δx is $\simeq -1.3$, in very good agreement with the dimensional argument leading to Equation (18).

When the magnetic field achieves its saturation strength, Q_{tot} balances the fluctuation power delivered to the grid scale by nonlinear coupling with longer lengthscales in the MHD turbulence. At resolutions currently feasible, these couplings are non-local in the sense that the shortest wavelengths couple significantly to essentially all longer lengthscales; however, there is reason to think that in genuine MHD turbulence, where the dynamic range between stirring scale and dissipation scale is far greater, the dissipation scale actually decouples (Lesur & Longaretti 2010). Because all our simulations are in the regime in which all lengthscales couple directly to the grid scale, we write the rate at which longer scales couple to the dissipation scale as

$$H_{\text{nonlin}} = s\Omega \langle \delta B_{\text{tot}}^2 \rangle \beta^{-m}, \quad (19)$$

where $\langle \delta B_{\text{tot}}^2 \rangle$ is the total variance in the magnetic field. Nonlinear energy transfer occurs on the eddy turnover, i.e., dynamical, timescale and involves the entire fluctuating power. Equating H_{nonlin} to Q_{tot} yields the prediction

$$\delta B_{\text{tot}} = \left[(8\pi)^m \frac{\Gamma q}{s} \frac{p_0^{m+3/4}}{\Sigma \Omega^2 \Delta x_0} \frac{f_{\text{grid}}^{5/2}}{(\Delta x / \Delta x_0)^{m+1-3k/4}} \right]^{1/(2m-1/2)}. \quad (20)$$

Here we have introduced the adiabatic index Γ , column density Σ , orbital frequency Ω , characteristic pressure p_0 , and grid resolution Δx_0 for which $p = p_0$. We have also introduced the quantity f_{grid} , the ratio between the characteristic amplitude of magnetic field fluctuations on the grid scale and on the stirring scale.

As the cell-size Δx decreases, we can expect f_{grid} to decrease. However, only when convergence is reached must it scale $\propto \Delta x^{m+1-3k/4}$. Consequently, convergence in the magnetic field intensity may not be monotonic. Using the data in our stratified shearing box calculations, we can measure how far toward convergence we have progressed in this regard by computing f_{grid} . Combining the Simon et al. and Davis et al. data, we find that f_{grid} falls from 0.42 for the simulation with 8 cells per scale height to 0.26 when there are 128 cells per H . In other words, for these simulations, in which $k = 0$ and the resolution

improves by a factor of 16, f_{grid} falls by only 40% so that, if the index $m = 0$, the ratio $f_{\text{grid}}^{5/2}/(\Delta x/\Delta x_0)^{m+1-3k/4}$ would rise by almost a factor of 5 and the saturated field strength would fall by a factor of 25. That the saturated magnetic field in fact increases, but rather slowly, over this range of resolutions suggests that $-1 \lesssim m \lesssim -0.5$; in other words, the nonlinear energy transfer rate increases as the gas pressure rises relative to the magnetic pressure. With this dependence of the nonlinear energy transfer rate on the plasma β , the saturated field strength increases as the gridscale fluctuations become smaller relative to the total variance. At still finer resolution, the scaling with Δx of both f_{grid} and the nonlinear coupling could change, but at least in this range of resolutions for these algorithms, the field intensity can be expected to grow with further refinement in spatial grids.

Thus, the action of gridscale dissipation creates a direct relation between resolution and the nonlinear processes that determine the magnetic field intensity and Maxwell stress. Because improving resolution also increases short lengthscale fluctuation power, the level of gridscale fluctuations diminishes only slowly with improving resolution. If, as appears to be the case in the simulations we have studied, nonlinear coupling between large scales and small grows modestly with an increasing ratio of gas pressure to magnetic pressure, the net result is a slow increase in saturated magnetic intensity with improving resolution. Processes like these account, at least in part, for the more stringent requirements for resolution that we have uncovered.

5.7. Difficulties of convergence testing

Although convergence testing is an accepted approach for gauging the reliability of numerical simulations, there are several issues that make it extremely difficult to apply to global accretion simulations. Some of these difficulties are practical; others are more fundamental.

One of the fundamental difficulties arises because accretion is driven by MHD turbulence, and the interaction of dynamics at widely-differing lengthscales is intrinsic to the nature of turbulence. Large dynamic range in spatial scales generically demands very high resolution, of course. The difficulties associated with achieving convergence are especially compounded for MRI-driven MHD turbulence for which stirring occurs over a wide range of scales. Lesur & Longaretti (2010) argue that a clearly defined inertial range separating the stirring scale from the dissipation scale still has not emerged in the shearing box, even at the highest resolution available to their spectral code. Because the total Maxwell stress is dominated by field energy on the largest scales, one may hope that its magnitude becomes reasonably well-determined even while the resolution remains insufficient to describe details

of the short-wavelength dissipation, but that remains to be demonstrated. The previous subsection discussed some of the problems to overcome in order to achieve that decoupling.

Among the practical considerations is that MHD turbulence-driven global accretion simulations must be three dimensional. Achieving even modest resolution in three dimensions requires a large number of cells. Whenever the science pushes computational capacity to its limit, it is infeasible to carry out additional simulations at higher resolution than the level at which one begins to see interesting effects. For this reason, attempts are sometimes made to “test convergence” by contrasting one set of results with those found at coarser resolution. Although this may be the only available procedure for simulations carried out at the largest feasible resolution, it is an approach that must be used with caution. If the gridscale at *every* resolution tested remains too coarse to be sensitive to a physical mechanism, the results will give the appearance of convergence, even while missing the very existence of a mechanism that may be very important. This motivates this paper: using the better-resolved shearing box simulations to develop diagnostics that allow a global simulation to be evaluated directly.

Finally, there is the difficulty of measuring the effects of truncation error and the rate at which it is being reduced for simulations carried out at relatively coarse, but practical, numerical resolutions. Strictly speaking, every algorithm has its own properties, particularly with respect to truncation error. Truncation error is characterized by the amplitude of the error, the effective convergence rate at a given resolution, and the asymptotic convergence rate. The latter is a fundamental property of the method, but in practice one almost never reaches the asymptotic regime, except in select test problems or for one-dimensional problems where exceptionally fine resolution may be achieved. At resolution levels reached in typical three-dimensional simulations, the observed convergence rate need not agree with the asymptotic convergence rate of the algorithm. Also, the convergence rate alone provides no information about the amplitude of the truncation error at a given resolution. Again, by determining properties that are characteristic of well-developed MRI-driven MHD turbulence (e.g., $\langle B_R^2/B_\phi^2 \rangle$), we sidestep this difficulty.

Both global and local simulations have made use of several different algorithms (finite-difference: *Zeus*, GRMHD; finite-volume conservative: *Athena*, HARM3D), as well as variations within the same general algorithm (e.g., different flux solvers). The relative merits of different algorithms will be reflected in the value of the Q parameters required to produce good results. For the shearing box results in § 3, we found that the use of either *Zeus* or *Athena* appears to make relatively little difference; our diagnostics of convergence depend upon resolution in very similar ways. In § 6 we compute the number of grid zones that might be required for a future well-resolved global simulation. These numbers can vary for one algorithm compared to another, according to the Q values that prove necessary.

5.8. Spatial resolution requirements and published global simulations

There is no single number by which spatial resolution may be defined. Even to specify the raw cell count requires three numbers, one for each dimension, and that is not sufficient because cell size depends on the extent of the simulation volume. Moreover, what really matters is not so much the absolute size of the cells as their size relative to the natural lengthscales of the problem. For global simulations, the radius R is the primary scale relevant to the radial direction, so the appropriate measure of cell size is $\Delta R/R$. In the azimuthal direction, there are two natural scales: radians and $2\pi v_{A\phi}/\Omega$. The former is due to the necessity of resolving a wide-range of non-axisymmetric modes in the turbulence; the latter has to do with adequate resolution for the fastest-growing linear non-axisymmetric modes. In the vertical direction, there are likewise two scales: the density (or pressure) scale height, H , and $2\pi v_{Az}/\Omega$. Quantities based on the Alfvén speed always require time-averaging because the field evolves rapidly over the course of the simulation; depending on the treatment of thermodynamics in the simulation, the vertical scale height may also require averaging. Therefore, to align resolution metrics against simulations in the literature requires translation of all cell-size specifications into these five natural units.

We have done this for a selection of published simulations in Table 4. In addition to cell size data, we list the radius of the pressure maximum in the initial torus used, and the simulation length in terms of orbits at that radius. The data from the various simulations reported here with the L, M, and R grids are also given in this table. The additional simulations used are: the high-resolution poloidal-field simulation of Hawley & Krolik (2002), which we label HK02; the high-resolution Schwarzschild simulation of De Villiers et al. (2003), called KD0b; the quadrupolar field simulation from Beckwith et al. (2008b), designated QD0; the high-resolution thinnest simulation of Noble et al. (2010), which they labeled ThinHR; the Schwarzschild simulation reported by Shafee et al. (2008), identified as “Shafee” in the table; and the fiducial simulation A0HR07 from Penna et al. (2010), here called “Penna”. For many of these, the published paper did not report full information. For those for which we have access to the data, we have computed what we needed; for the remainder, we have filled in only those entries derivable from the publications. Where this required reading values off graphs, we have added a question mark. All but one of the simulations listed in the table used an azimuthal range of $\pi/2$; the Shafee simulation used a wedge only $\pi/4$ in angle. In these other simulations, unlike the *Zeus* simulations described in this paper, the radial grid has a fixed $\Delta R/R$. They also differ in that, unlike our new *Zeus* simulations, which used cylindrical coordinates, they used spherical coordinates. Because $\Delta z = R\Delta\theta$ in spherical coordinates, the radial gradients in $\langle Q_z \rangle$ seen in the *Zeus* simulations are greatly reduced.

As the data in this table demonstrate, most global simulations performed hitherto have

had effective resolutions roughly at the level of our M grid with the standard azimuthal resolution, while the Penna simulation most closely resembled our twoloop-1000-mlp simulation, which used our poloidal M grid but coarser azimuthal resolution. As a fraction of the local radius, the radial cell sizes have been generally in the range $\simeq 0.01$ – 0.025 , similar to the 0.017 – 0.055 range of our M grid; the only exceptions in this list are Shafee ($\Delta R/R = 0.0065$) and ThinHR ($\Delta R/R = 0.004$), both of whose radial resolution was closer to our R grid. In terms of the scale height, the vertical cells of most of these simulations are in the range 0.02 – 0.14 , again matching our M grid; by this measure, Shafee is similar to all the others, while ThinHR is the only one substantially better, with $\Delta z/H = 0.0086$. These values match the range explored in the stratified shearing box simulations, where the coarsest we discussed had a vertical cell $0.125H$ thick, and the thickness of the finest vertical cell was $0.0078H$. In radian measure, all of these simulations except Penna used a cell with $\Delta\phi = 0.025$, identical to that in our standard M grid; Penna’s azimuthal cell was twice as large. Our ability to be quantitative about $\langle Q_z \rangle$ and $\langle Q_\phi \rangle$ is limited: we kept insufficient data from HK02 to compute these diagnostics, and we lack access to data from Shafee and Penna. However, on the basis of what the published papers say, it is clear that $\langle Q_z \rangle$ in most of the global disk literature has been $\simeq 5$ – 8 , while $\langle Q_\phi \rangle$ has been $\simeq 20$. By these measures, at $\simeq 25$, ThinHR was a lone standout in terms of $\langle Q_z \rangle$, but in the same range as all the others in terms of $\langle Q_\phi \rangle$.

Because our M and R grid simulations at best went only part way toward convergence as measured by any of our diagnostics, we expect that all these simulations likewise fell short of convergence. For those cases in which the initial magnetic field was in a single dipole loop (HK02, KD0b), the $\langle Q_z \rangle$ values suggest that the $\langle B_R^2/B_\phi^2 \rangle$ measure is in the neighborhood of $\sim 1/2$ its saturated value. For those in which the initial magnetic field was in two loops (QD0b, Shafee), the shift we have seen in 2-loop simulations relative to 1-loop suggests that $\langle B_R^2/B_\phi^2 \rangle$ is somewhat smaller. The Shafee simulation also has large

Table 4. Cell-sizes

Name	$\Delta R/R$	$\Delta\phi$	$\langle Q_\phi \rangle$	$\Delta z/H$	$\langle Q_z \rangle$	R_{max}	Orbits
L Grid	0.033–0.111	0.025	7–10	0.0333–0.1	1–3	35	33
M Grid	0.017–0.055	0.025	$\simeq 10$	0.016–0.08	2–10	35	54
R Grid	0.004–0.0067	0.025	6–12	0.02–0.1	3–10	35	28
HK02	0.008–0.015	0.025		0.02–0.07		20	15
KD0b	0.024	0.025	19	0.06–0.14	6	25	14
QD0	0.024	0.025	26	0.08	8	25	14
ThinHR	0.004	0.025	18	0.0086	25	35	12
Shafee	0.0065	0.025		0.03		35	8
Penna	0.013	0.05		0.064	$\sim 5?$	35	22

aspect ratio cells (although $\Delta R/(R\Delta\phi)$ is similar in ThinHR, the latter’s much finer vertical resolution appears to compensate). In Penna, the combination of a four-loop configuration and coarser azimuthal resolution seems particularly challenging. In our simulations such conditions cause $\langle B_R^2/B_\phi^2 \rangle$ to fall by a factor of 2 or more. Such a reduction in the relative magnitude of the radial component of the magnetic field would indicate that the turbulence is not fully developed, that the field intensity is rather lower than the converged value, and that the stress is smaller than in saturation because it is proportional to B_R .

6. Conclusions

Although global disk simulations have explored many important aspects of the accretion process, their quantitative reliability remains uncertain. In this paper we have made use of high resolution local shearing box simulations to develop four diagnostics by which one may gauge how closely a given simulation approaches to fully developed MRI-driven MHD turbulence. We have then examined how those diagnostics carry over to global simulations. Establishing this connection is an important step in relating local simulations to global. Local simulations will always be able to include more physics and use better effective resolution than global, and by means of this mutual calibration, information from shearing boxes can help guide and interpret global models.

These four are: $\langle Q_z \rangle$, the number of vertical cells across a wavelength of the fastest-growing poloidal field MRI mode; $\langle Q_y \rangle$ (or $\langle Q_\phi \rangle$ in global simulations), the number of azimuthal cells across a wavelength of the fastest-growing toroidal field MRI mode; $\langle B_R^2/B_\phi^2 \rangle$, the ratio of energy in the radial magnetic field component to the toroidal component; and α_{mag} , the ratio of the Maxwell stress to the magnetic pressure. Only the first has seen significant use previously, and we extend its utility to gauge spatial resolution for nonlinear behavior of the MHD turbulence as well as linear growth of the MRI. Whereas Sano et al. (2004) found that a minimum $\langle Q_z \rangle$ of 6–8 is required in order to describe poloidal MRI linear growth, we find that the prerequisite for simulating nonlinear behavior is more stringent and couples poloidal resolution to azimuthal. If the analogous azimuthal diagnostic $\langle Q_\phi \rangle \gtrsim 20$, then $\langle Q_z \rangle \gtrsim 10$ is necessary; if $\langle Q_\phi \rangle$ is smaller than that, still larger values of $\langle Q_z \rangle$ are required.

Using these diagnostics, we find that all the global simulations done to date are under-resolved, particularly in the ϕ direction. Only one simulation in the literature (ThinHR, Noble et al. 2010) comes close to adequate poloidal resolution, but even it does not meet the azimuthal standard. Our tests varying the azimuthal cell-size showed that it can be important to the development of the poloidal, as well as the toroidal, magnetic field. Achieving

adequate azimuthal resolution is made especially difficult when the disk is thin for two reasons. Thinner disks require smaller vertical cell dimensions, but avoiding the deleterious effects of large cell aspect ratios then demands cells still smaller in the azimuthal direction. In addition, v_A tends to diminish with the smaller sound speeds seen in thinner disks; smaller $\Delta\phi$ is then necessary in order to achieve an adequate value of Q_ϕ .

Regarding the initial conditions, we have found that the additional short lengthscale fluctuation power that is a concomitant of more complicated magnetic field geometry places stronger demands on spatial resolution. The additional magnetic reconnection associated with attempting to describe a more complicated field geometry on a given grid can weaken the field sufficiently that MRI stirring is curtailed and the field intensity remains artificially low. Until global simulations are adequately resolved it will be difficult to distinguish numerical from physical effects arising from different initial field geometries.

We can make an estimate of the resolution required for a global torus evolution using Equations (11) and (13). To avoid the problem of decreasing H with decreasing R that is found in cylindrical coordinates, we assume a spherical-polar grid (r, θ, ϕ) . To keep $\Delta r = r\Delta\phi$ we use logarithmic spacing in r . We also assume the radial grid spans a factor of 100 from the inner to the outer boundary, and that the ϕ grid spans only $\pi/2$. We next assume $\beta = 10$, $\beta_z/\beta = 50$, $H/R = 0.1$. Our target values are $\langle Q_z \rangle = 10$ and $\langle Q_\phi \rangle = 25$ (one's preferred target Q values may well be algorithm dependent). With these assumptions, the θ grid, if equally spaced, must have ~ 900 zones if equally spaced from 0 to π . In a practical simulation, however, one could increase $\Delta\theta$ away from the midplane, reducing the number of zones required, perhaps by as much as 50% (450 zones). The ϕ grid requires 200 zones and the r grid 600 zones. For $H/R = 0.1$, the number of cells ($600 \times 200 \times 450$) is not too much greater than what has already been used. Of course, reducing H/R would further increase the number of required zones proportionally in each of the three dimensions. Higher resolution also reduces the Courant-limited timestep, making it challenging to evolve the disk for a large number of orbits. In this estimate we assumed a smooth distribution of field; intermittency in the field distribution may change the required resolution from this estimate. Typically there is significant spatial variation in β so that a density weighted Q value can be larger than a volume-weighted value. On the other hand, complex initial field distributions may require more zones for adequate representation. Future simulations done at resolutions approaching this estimate can test these ideas.

Although we find that certain values of the resolution parameters indicate well-resolved turbulence, lower values of those parameters don't mean that turbulence necessarily decays rapidly; as we have described, it can persist for long periods of time with lower amplitude and reduced stress. Even under-resolved global simulations can have nonzero stress levels

and accretion rates. A seemingly long duration of accretion is therefore *not* a guarantor of convergence. Qualitative conclusions can usefully be—and have been—obtained from such simulations, but quantitative stress levels are likely to be undervalued.

Lastly, we have explored the question of the meaning of “inflow equilibrium” in the context of global simulations. Analysis of several diagnostics can determine the existence and extent of the region of the accretion disk that is in inflow equilibrium. One can show that there are at most weak long-term trends in the radial mass distribution, that the time-averaged accretion rate is relatively constant as a function of R , and that the observed accretion rate is consistent with the observed angular momentum transport as computed from the steady-state disk equation. Even when the disk is in time-averaged inflow equilibrium, there can be large short-term fluctuations in the mass distribution. Moreover, whenever there is only a finite mass reservoir in the initial condition, a sufficiently long simulation cannot, by definition, support even a statistical steady-state for longer than the inflow time from the initial half-mass radius.

In summary, this work provides guidance for future global simulations, both in terms of resolution and evolution time, to approach what is needed for quantitative conclusions about accretion disk dynamics and structure.

Acknowledgements

This work was partially supported by NASA grant NNX09AD14G and NSF grant AST-0908869 (JFH) and NSF grant AST-0908336 (JHK). Some of the simulations described here were carried out the Ranger system at TACC and on the Kraken system at NICS, both supported by the NSF. We thank Jake Simon, Shane Davis and Jim Stone for sharing data from their shearing box simulations, and Simon, Stone and Kris Beckwith for comments on the manuscript.

REFERENCES

- Anninos, P., Fragile, P. C., & Salmonson, J. D. 2005, *ApJ*, 635, 723
- Balbus, S. A. & Hawley, J. F. 1991, *ApJ*, 376, 214
- . 1992, *ApJ*, 400, 610
- . 1998, *Reviews of Modern Physics*, 70, 1

- Beckwith, K., Hawley, J. F., & Krolik, J. H. 2008a, *ApJ*, 678, 1180
- . 2008b, *MNRAS*, 390, 21
- . 2009, *ApJ*, 707, 428
- Blackman, E. G., Penna, R. F., & Varnière, P. 2008, *New Astronomy*, 13, 244
- Brandenburg, A., Nordlund, A., Stein, R. F., & Torkelsson, U. 1995, *ApJ*, 446, 741
- Davis, S. W., Stone, J. M., & Pessah, M. E. 2010, *ApJ*, 713, 51
- De Villiers, J., Hawley, J. F., & Krolik, J. H. 2003, *ApJ*, 599, 1238
- De Villiers, J., Hawley, J. F., Krolik, J. H., & Hirose, S. 2005, *ApJ*, 620, 878
- De Villiers, J.-P. & Hawley, J. F. 2003, *ApJ*, 589, 458
- Fleming, T. P., Stone, J. M., & Hawley, J. F. 2000, *ApJ*, 530, 464
- Fromang, S. & Papaloizou, J. 2007, *A & A*, 476, 1113
- Fromang, S., Papaloizou, J., Lesur, G., & Heinemann, T. 2007, *A & A*, 476, 1123
- Gammie, C. F., McKinney, J. C., & Tóth, G. 2003, *ApJ*, 589, 444
- Guan, X. & Gammie, C. F. 2011, *ApJ*, 728, 130
- Hawley, J. F., Gammie, C. F., & Balbus, S. A. 1995, *ApJ*, 440, 742
- . 1996, *ApJ*, 464, 690
- Hawley, J. F. & Krolik, J. H. 2001, *ApJ*, 548, 348
- . 2002, *ApJ*, 566, 164
- Hirose, S., Krolik, J. H., & Blaes, O. 2009, *ApJ*, 691, 16
- Hirose, S., Krolik, J. H., & Stone, J. M. 2006, *ApJ*, 640, 901
- Lesur, G. & Longaretti, P. 2007, *MNRAS*, 378, 1471
- . 2010, *ArXiv e-prints*
- Machida, M. & Matsumoto, R. 2003, *ApJ*, 585, 429
- McKinney, J. C. & Gammie, C. F. 2004, *ApJ*, 611, 977

- Miller, K. A. & Stone, J. M. 2000, *ApJ*, 534, 398
- Noble, S. C., Krolik, J. H., & Hawley, J. F. 2009, *ApJ*, 692, 411
- . 2010, *ApJ*, 711, 959
- Oishi, J. & MacLow, M.-M. 2011, *ApJ*
- Penna, R. F., McKinney, J. C., Narayan, R., Tchekhovskoy, A., Shafee, R., & McClintock, J. E. 2010, *MNRAS*, 1216
- Sano, T. & Inutsuka, S. 2001, *ApJ*, 561, L179
- Sano, T., Inutsuka, S., Turner, N. J., & Stone, J. M. 2004, *ApJ*, 605, 321
- Sano, T. & Stone, J. M. 2002, *ApJ*, 577, 534
- Schnittman, J. D., Krolik, J. H., & Hawley, J. F. 2006, *ApJ*, 651, 1031
- Shafee, R., McKinney, J. C., Narayan, R., Tchekhovskoy, A., Gammie, C. F., & McClintock, J. E. 2008, *ApJ*, 687, L25
- Shakura, N. I. & Sunyaev, R. A. 1973, *A & A*, 24, 337
- Shi, J., Krolik, J. H., & Hirose, S. 2010, *ApJ*, 708, 1716
- Simon, J. B., Hawley, J. F., & Beckwith, K. 2009, *ApJ*, 690, 974
- . 2011, *ApJ*, 730, 94
- Sorathia, K. A., Reynolds, C. S., & Armitage, P. J. 2010, *ApJ*, 712, 1241
- Stone, J. M. 2009, in *Astronomical Society of the Pacific Conference Series*, Vol. 406, *Astronomical Society of the Pacific Conference Series*, ed. N. V. Pogorelov, E. Audit, P. Colella, & G. P. Zank, 277–+
- Stone, J. M. & Gardiner, T. A. 2010, *ApJS*, 189, 142
- Stone, J. M., Gardiner, T. A., Teuben, P., Hawley, J. F., & Simon, J. B. 2008, *ApJS*, 178, 137
- Stone, J. M., Hawley, J. F., Gammie, C. F., & Balbus, S. A. 1996, *ApJ*, 463, 656
- Stone, J. M. & Norman, M. L. 1992, *ApJS*, 80, 753
- Winters, W. F., Balbus, S. A., & Hawley, J. F. 2003, *MNRAS*, 340, 519

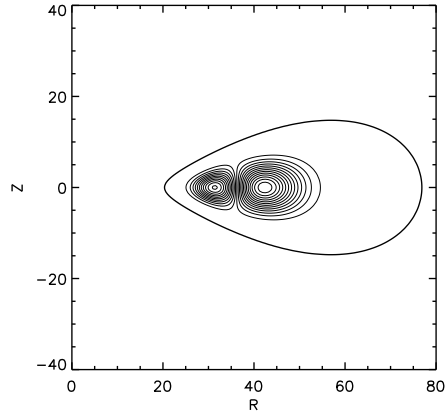


Fig. 1.— Initial torus and field configuration for the two-loop simulations. The outermost contour line marks the boundary of the initial torus. The remaining contours are the magnetic field lines.

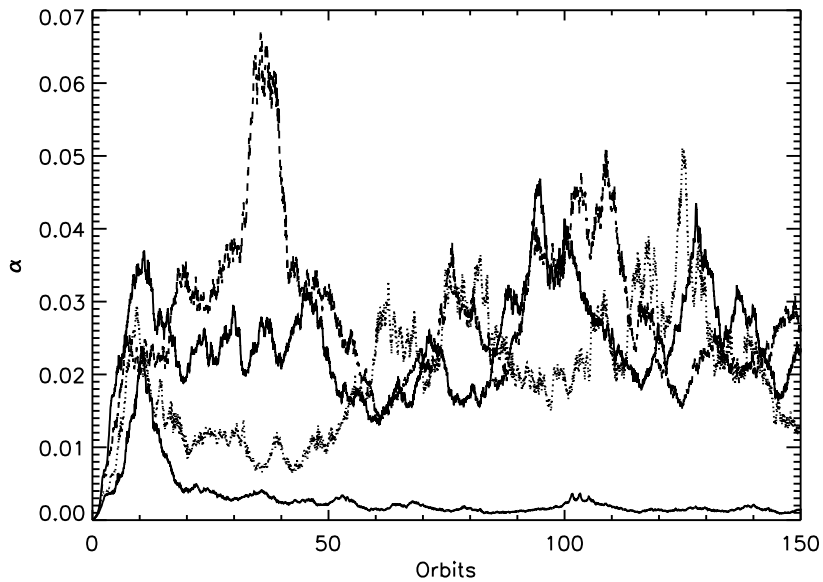


Fig. 2.— Ratio of α , the volume-averaged Maxwell and Reynolds stress to volume-averaged pressure in a set of four stratified shearing box simulations. The simulations use 8 (lowest solid line), 16 (dotted line), 32 (dashed line), and 64 zones (solid line) per scale-height H .

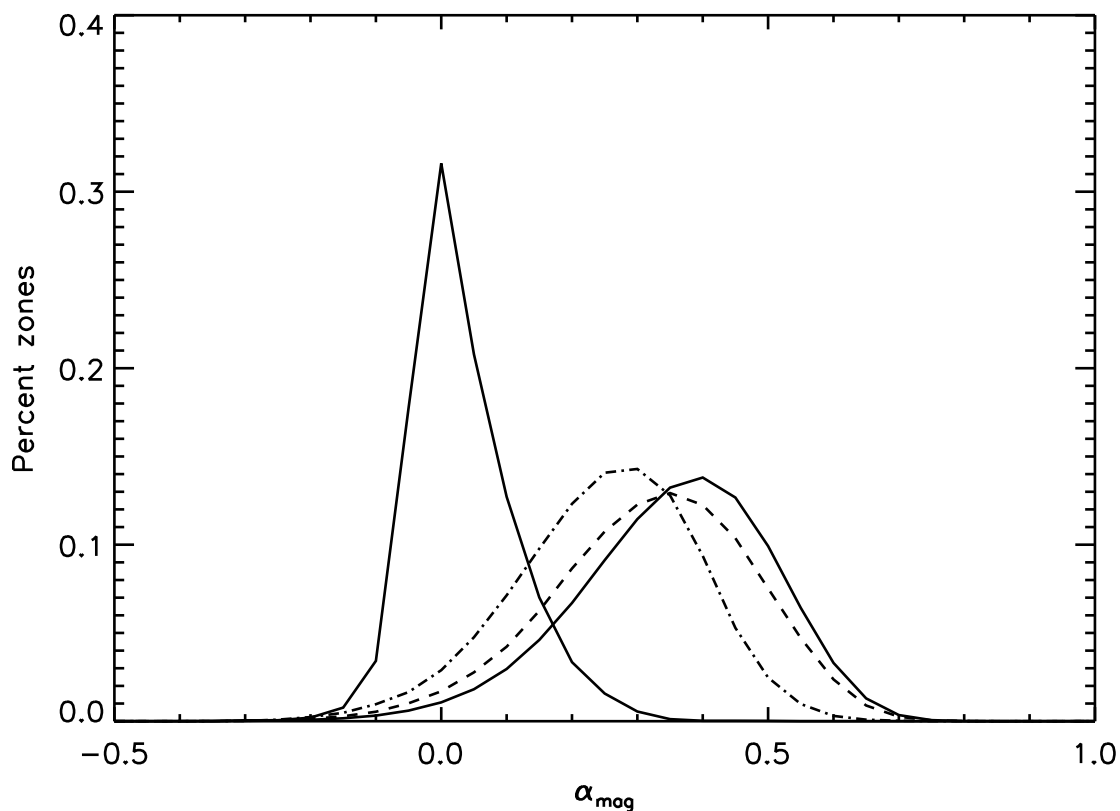


Fig. 3.— Distribution function for the time- and volume-averaged ratio of the Maxwell stress to the magnetic pressure, α_{mag} taken from a set of four stratified shearing box simulations using 8 (left-most solid line), 16 (dot-dashed line), 32 (dashed line), and 64 zones (solid line) per scale-height H . As resolution increases the peak of the distribution of α_{mag} shifts to higher values.

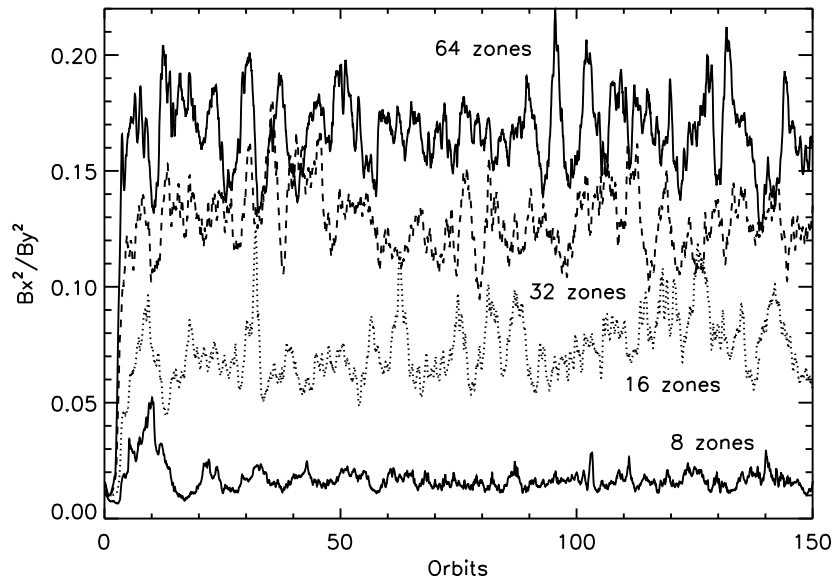


Fig. 4.— Ratio of volume-averaged radial to toroidal field energies, $\langle B_x^2 \rangle / \langle B_y^2 \rangle$ for stratified shearing box simulations using 8 (solid line), 16 (dotted line), 32 (dashed line), and 64 zones (solid line) per scale-height H . This ratio shows a systematic increase with resolution.

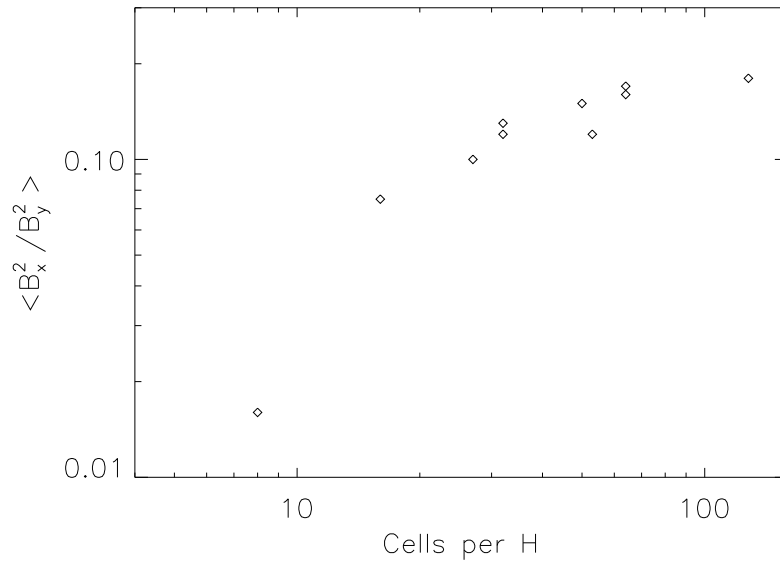


Fig. 5.— Ratio of the volume-averaged radial field energy to toroidal field energy, $\langle B_x^2 / B_y^2 \rangle$ as a function of resolution in stratified shearing box simulations. Resolution is measured in number of grid cells per scale-height H .

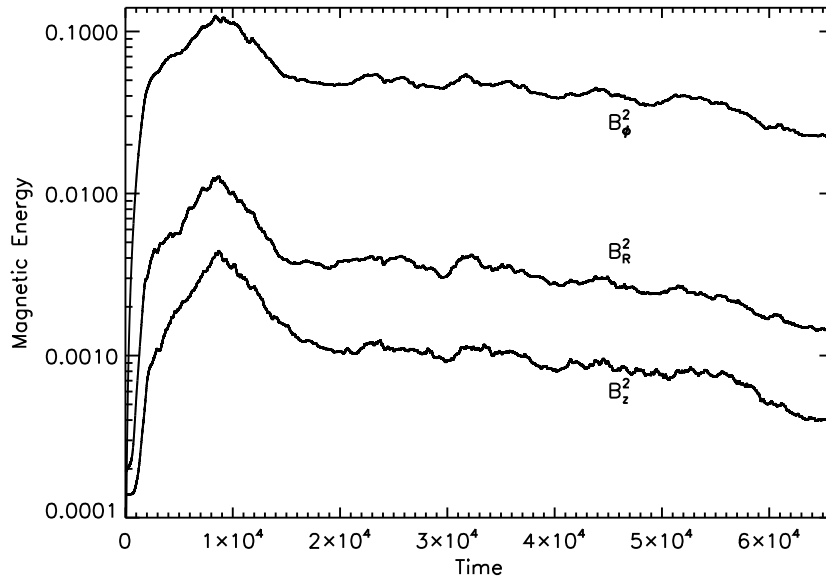


Fig. 6.— Evolution of the three components of the magnetic energy as a function of time in the fiducial simulation, twoloop-1000-mr.

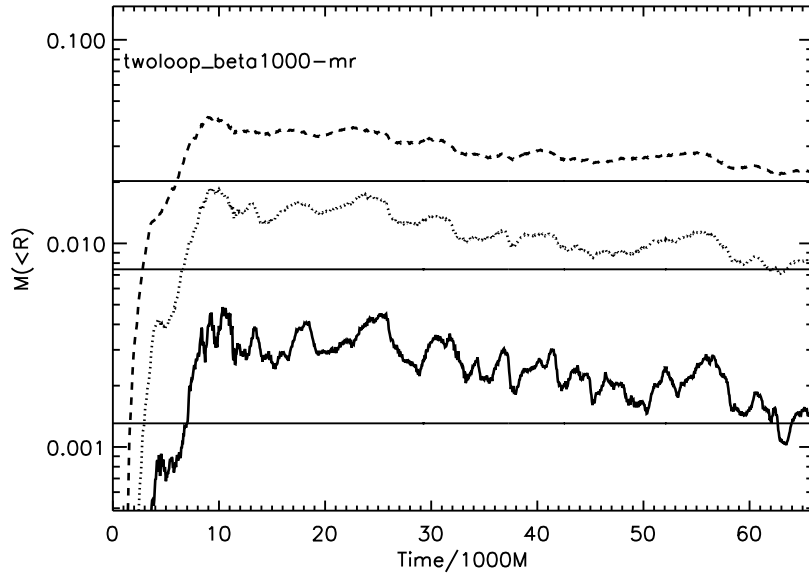


Fig. 7.— The mass interior to three radii ($R = 10M$: solid, $R = 15M$: dotted, $R = 20M$: dashed) as a function of time in the fiducial simulation. Mass units are fraction of the total initial mass. The time averaged accretion rate, \dot{M} , is 1% of the initial mass every $3700M$ in time.

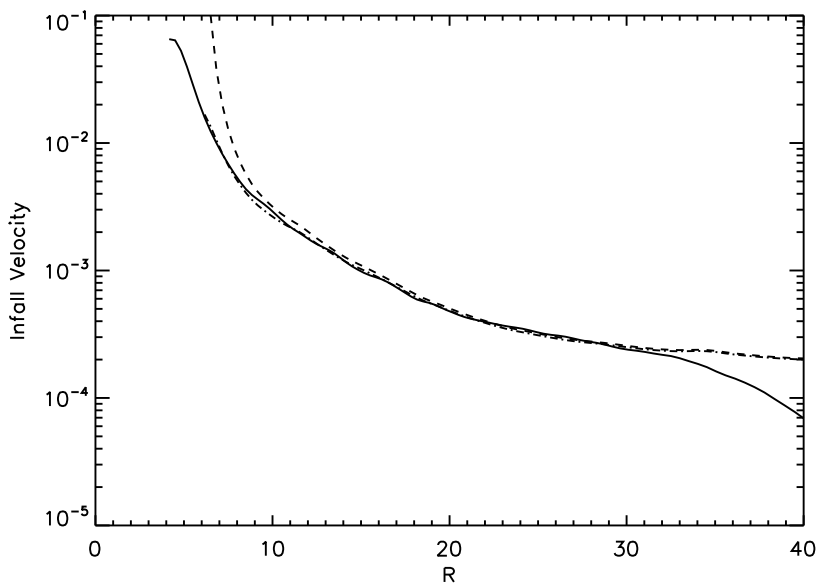


Fig. 8.— The inflow velocity for the fiducial run derived from the vertically and azimuthally integrated accretion rate and density (solid line), along with the inflow velocity derived from the vertically and azimuthally averaged Maxwell stress, pressure and accretion rate using a steady state disk approximation (dashed line) with $j_* = j_{ISCO}$. The dot-dashed line is the steady state inflow velocity derived using $j_* = 0.985j_{ISCO}$. The data are time-averaged from $t = 4-5 \times 10^4 M$.

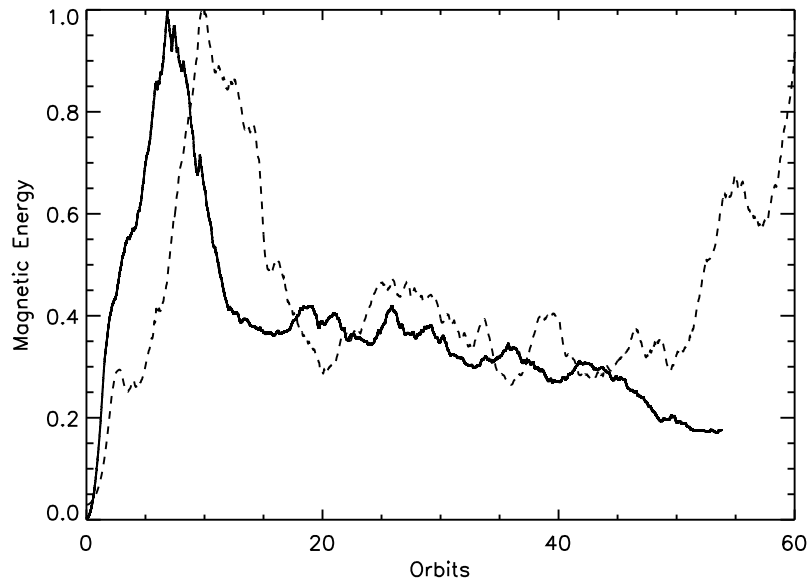


Fig. 9.— Evolution of the magnetic energy in the fiducial run (solid line) compared to the magnetic energy in a stratified shearing box simulation with 16 zones per H (dashed line). Time is orbits at the initial torus pressure maximum or in terms of the shearing box Ω , and the magnetic energies are normalized to their peak value. Both models show a period of rapid field amplification followed by a peak and a decline to a longer-term value that slowly declines. The magnetic energy increases after 50 orbits in the shearing box, but not in the global model.

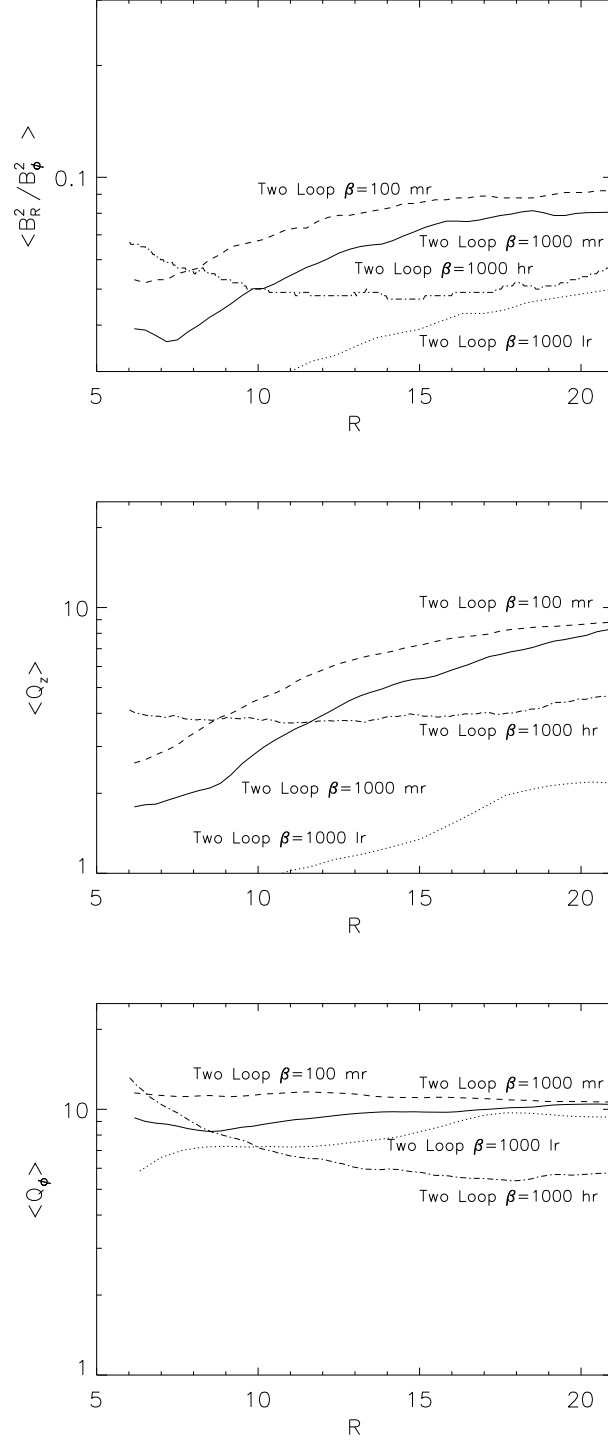


Fig. 10.— Radial dependence of the principal diagnostics for the 2-loop simulations with the standard azimuthal resolution. The curves are labeled with model name. The data were averaged over azimuth and height with a density weighting and then averaged in time from $2\text{--}3.4 \times 10^4 M$ for all three simulations. (Top) $\langle B_R^2 / B_\phi^2 \rangle$, (Middle) $\langle Q_z \rangle$, (Bottom) $\langle Q_\phi \rangle$.

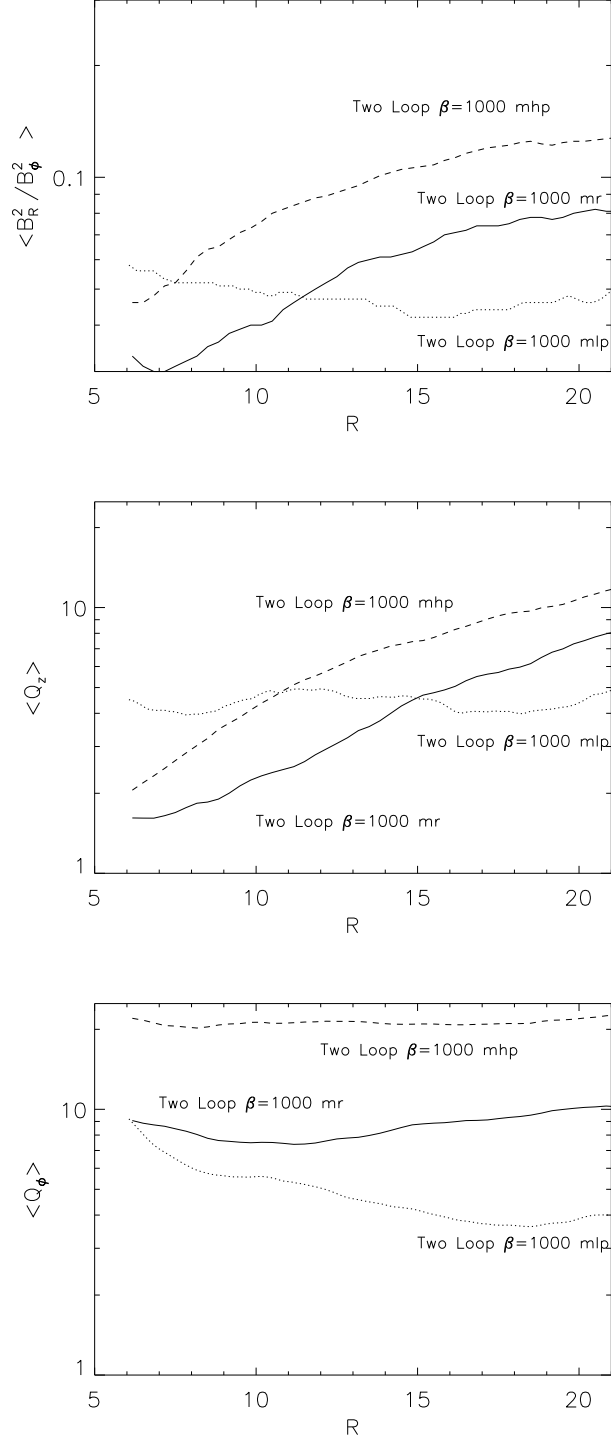


Fig. 11.— Radial dependence of the principal diagnostics for the 2-loop simulations with varying azimuthal resolution. The lines are labeled with model name. The data were averaged over azimuth and height with a density weighting and then averaged in time from $1.8\text{--}2.5 \times 10^4 M$ for all three simulations. (Top) $\langle B_R^2 / B_\phi^2 \rangle$, (Middle) $\langle Q_z \rangle$, (Bottom) $\langle Q_\phi \rangle$.

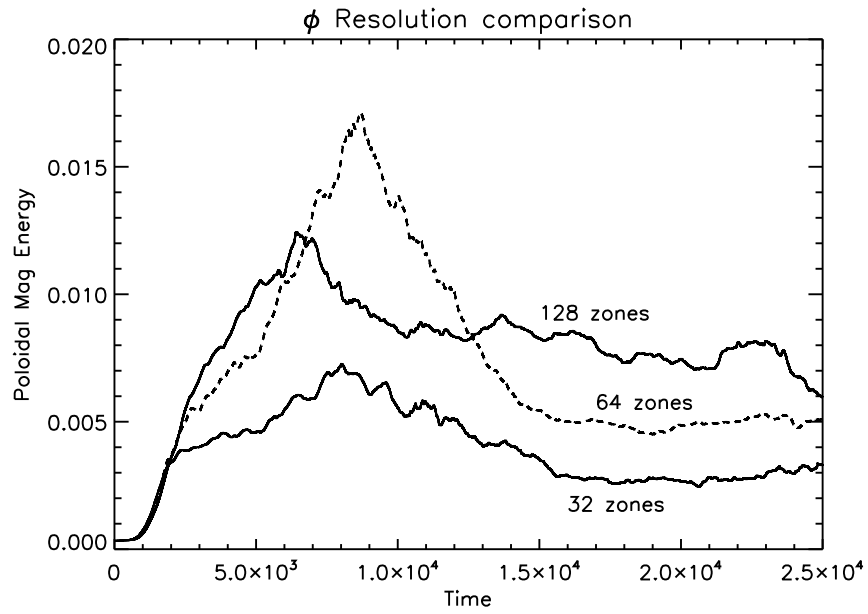


Fig. 12.— Evolution of three simulations using different numbers of zones to span the ϕ domain: 32, 64 (dashed line) and 128. The initial conditions were the same: two magnetic field loops with average strength $\beta = 1000$.

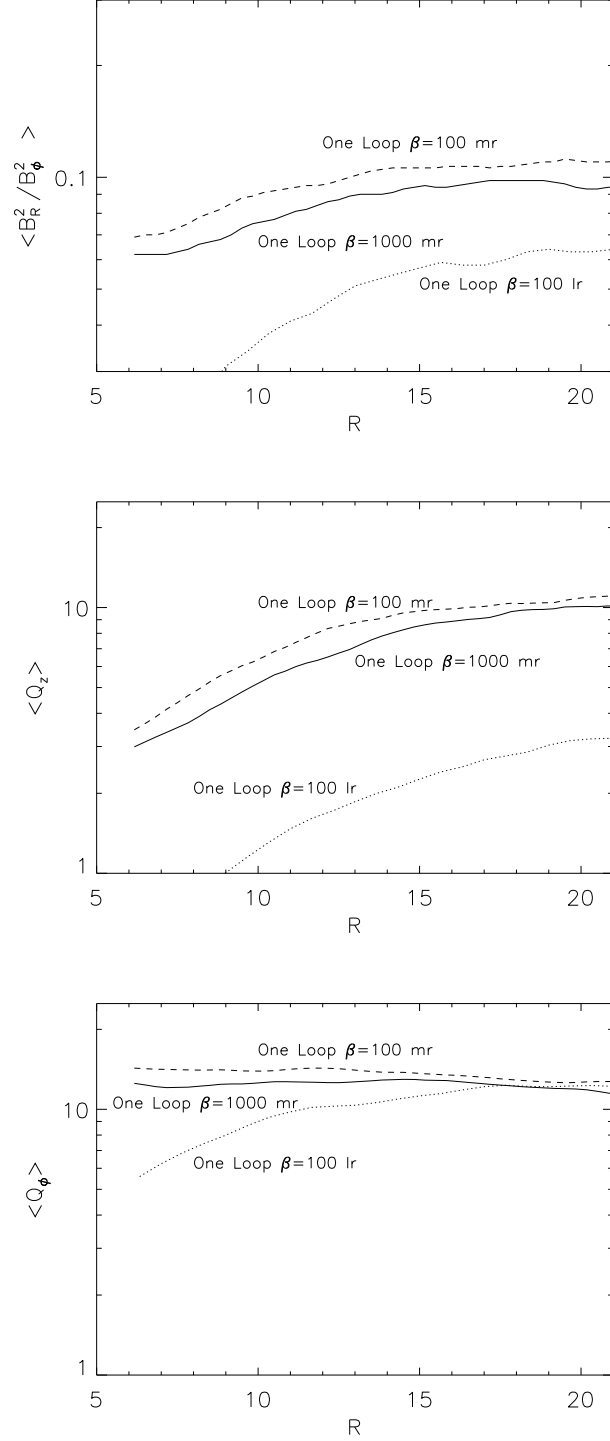


Fig. 13.— Radial dependence of the principal diagnostics for the 1-loop simulations with the standard azimuthal resolution. The curves are labeled with the corresponding model name. The data were averaged over azimuth and height with a density weighting and then averaged in time from $2\text{--}3.8 \times 10^4 M$ for all three simulations. (Top) $\langle B_R^2 / B_\phi^2 \rangle$. (Middle) $\langle Q_z \rangle$. (Bottom) $\langle Q_\phi \rangle$.

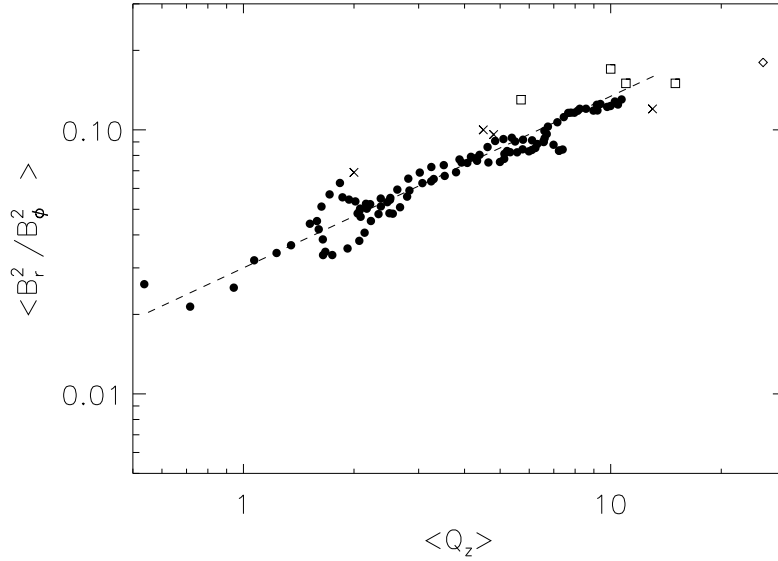


Fig. 14.— Correlation between $\langle Q_z \rangle$ and $\langle B_R^2 / B_\phi^2 \rangle$. The points shown by filled circles in this figure are drawn from the same set of times in three different simulations: twoloop-beta1000-lr, twoloop-beta1000-mr (the fiducial global simulation), and twoloop-beta1000-mhp. All are density-weighted averages, but they are taken at different radii within the inner disk. The points shown by the other symbols are time-averages of data from the midplane region of the shearing box simulations. The different symbols within this category denote different ranges of $\langle Q_y \rangle$: $12 \leq \langle Q_y \rangle \leq 25$ (x's); $25 < \langle Q_y \rangle \leq 50$ (squares); $\langle Q_y \rangle = 98$ (diamond). The dashed line has a slope of 0.65.

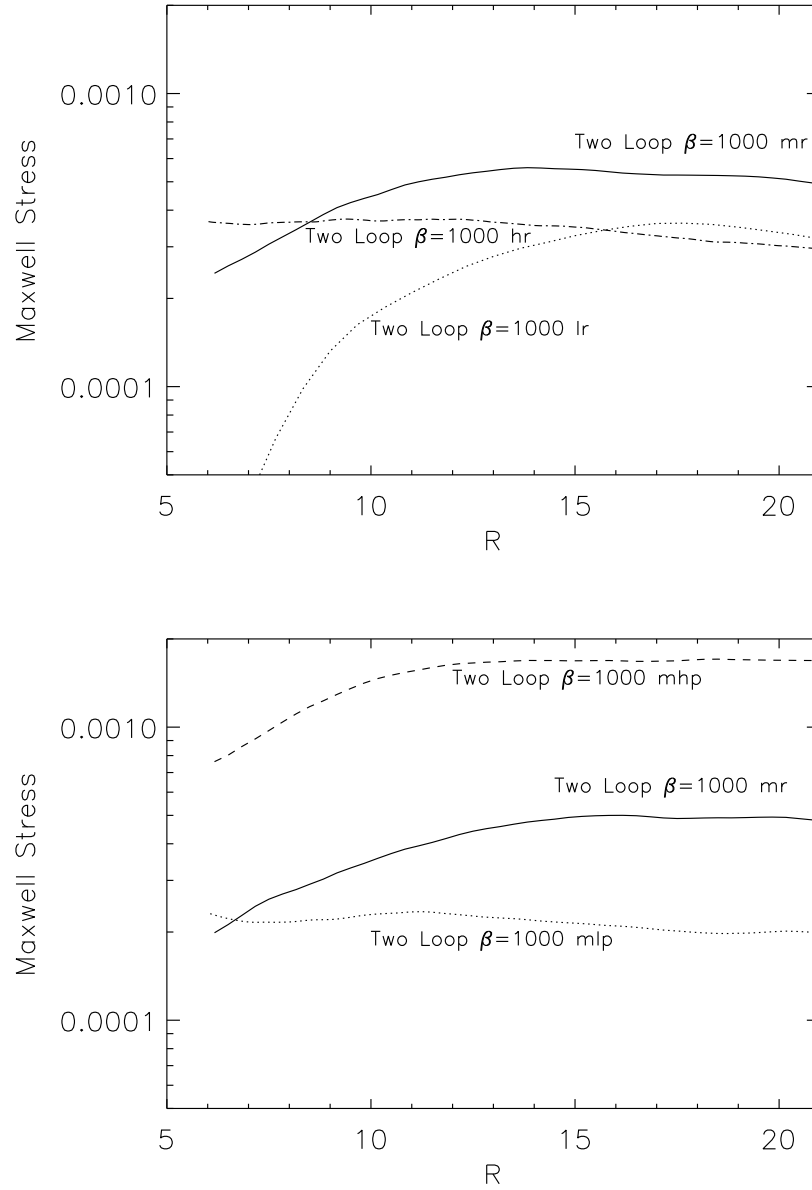


Fig. 15.— Time-averaged and shell-integrated Maxwell stress profiles for the three 2-loop simulations differing only in poloidal grid (Top) and the three 2-loop simulations differing only in azimuthal grid (Bottom). Curves are labeled by their model name.